Penalty C^0 8-node quadrilateral and 20-node hexahedral elements for consistent couple stress elasticity based on the unsymmetric finite element method

Huan-Pu Wu[1], Yan Shang[1, *], Song Cen[2, 3], Chen-Feng Li[4]

[1]*State Key Laboratory of Mechanics and Control of Mechanical Structures, Nanjing University of Aeronautics and Astronautics, Nanjing 210016, China*

[2]*School of Mechanics & Engineering, Liaoning Technical University, Fuxin 123000, China*

[3]*Department of Engineering Mechanics, School of Aerospace Engineering, Tsinghua University, Beijing 100084, China*

[4]*Zienkiewicz Centre for Computational Engineering and Energy Safety Research Institute, College of Engineering, Swansea University, Swansea SA1 8EN, UK*

*Corresponding author, E-mail: shangyan@nuaa.edu.cn

Abstract

In this paper, the penalty unsymmetric finite element framework for the consistent couple stress theory is derived from the virtual work principle. The C^1 continuity requirement is satisfied in weak form by using the penalty function method to constrain the independently introduced rotations for approximating the mechanical rotations, enabling the utilization of C^0 continuous interpolations for designing the element displacement without the loss of convergence property. Within the proposed framework, 8-node quadrilateral element and 20-node hexahedral solid element are constructed for analyzing the size-dependent mechanical responses of consistent couple stress elasticity materials. In these developments, the quadratic serendipity isoparametric shape functions are enriched by the rotation degrees of freedom for determining the test functions, whilst the metric stress functions that are derived from the concerned equilibrium equations are used to design the trial functions. A series of numerical benchmarks are examined for verifying their effectiveness and accuracy. It is shown that the elements can efficiently capture the size dependences, exhibiting good accuracy and low susceptibility to mesh distortion.

Key words: unsymmetric FEM; consistent couple stress theory; size dependence; mesh distortion; penalty function

1. Introduction

The couple stress theories [1-4] have been demonstrated in various applications as the effective approaches to predict the size-dependent mechanical behaviors of small-scale structures. Compared with other high-order continuum theories, such as the strain gradient theories [5-8] and nonlocal theories [9-11], the couple stress theories are popular due to their concise mathematical expressions and explicit physical interpretations. The first attempt to develop a mathematical continuum model with couple stress can be traced back to Cosserat brothers [12]. In their theory, the basic kinematical quantities are the displacements and independent material microrotations. It is noted that the usage of independent microrotations brings extraneous degrees of freedom and many additional material parameters, and the experimentally determination of these material parameters is a very challenging task. From the Cosserat model, by constraining the microrotation to be identical to the continuum mechanical rotation which is defined as one half of the curl of the displacement, Toupin [1], Mindlin and Tiersten [2], Koiter [3] explored the classical C^1 version of couple stress theory. Their theory is often referred to as the TMK-CST. In the developments, two intrinsic length scale parameters apart from two Lame's constants are required in the constitutive relationships to consider the microstructure effects of isotropic elastic materials. Afterwards, Yang et al. [13] established the modified couple stress theory (MCST) by postulating an artificial equilibrium condition of moments of couples to enforce the couple stress tensor to be symmetric but without presenting a convincing argument. The decisive advantage is that only the symmetrical parts of curvatures are considered and consequently, the number of the additional material length scale parameters for isotropic elastic materials is further reduced from two to one. In past decades, the MCST has drawn great attention and been successfully used to analyze many kinds of problems [14].

Recently, Hadjesfandiari and Dargush [4] proposed another version of the couple stress theory that requires only one additional length scale parameter for isotropic elastic materials. Different with the MSCT, the couple stress tensor in their theory is assumed to be skew-symmetric and conjugated to the mean curvature tensor which is defined as the skew-symmetric part of the gradient of the rotation. As reported in [4] that this theory can overcome the inconsistent deficiency which is primarily caused by the indeterminacy of the spherical part of the couple stress tensor in the original couple stress theory or modified couple stress theory, thus it is named by the consistent couple stress theory (CCST). One can find that the MCST and CCST are the two distinct cases degenerated from

the TMK-CST in some sense. Rizzi et al. [15] pointed out that these two theories coincide with each other in simple shear responses meanwhile differences are expected in other types of deformation. To date, there is still some debate as to which of these two theories is more appropriate [16, 17]. But this topic is beyond the scope of the present article.

Despite the controversy, the CCST has seen increasing use in the past few years owing to its simplicity and verifiability. For instance, Hadjesfandiari [18, 19] subsequently developed the size-dependent piezoelectricity and thermoelasticity theories based on the CCST; Alavi et al. [20] proposed the Timoshenko beam model based on the CCST using the extended Hamilton's principle; Patel et al. [21] analyzed the large deflection deformations of elastic cantilever microbeams based on the CCST; Li et al. [22] performed the size-dependent analysis of a microbeam considering the electromechanical coupling effects; Dehkordi and Beni [23] investigated the electromechanical vibration analysis of isotropic single-walled piezoelectric conic nanotubes using the Love's thin shell assumption; Subramaniam and Mondal [24] studied the influences of couple stresses on the rheology and dynamics of linear Maxwell viscoelastic fluids based on the CCST; Wu and Hu [25] proposed the unified size-dependent plate formulation of various shear deformation plate theories; Qu et al. [26] developed a high-frequency micro-plate model based on the CCST using the series expansion theory and analyzed the propagation property of straight-crested waves.

Although the theoretical investigations allow to provide an insight into the mechanism of micro/nano structures, the robust numerical methods play an important role in solving engineering problems with complex geometries and boundary conditions. As one of the most commonly used numerical tools for solids in science and engineering, the finite element method (FEM) has obviously become an appealing choice for this task. However, it's worth emphasizing that it is not easy to develop advanced finite elements with simple expression and satisfactory performance based on the C^1 couple stress theories due to the requirement of C^1 continuity to the displacement interpolation. In general, the C^1 continuity requirement inevitably makes the construction procedure of element quite tedious as well as makes the final formulation complicated [27]. In addition, it is well known that the precision of the FEM critically depends on the mesh quality and is very easily afflicted with the mesh distortion [28]. Unfortunately, this issue will be significantly exacerbated by the C^1 continuity requirement.

At present, there exists a variety of element models developed based on the MCST. We mention

the beam elements [29, 30], plate elements [31-33], shell elements [34, 35], two-dimensional (2D) elements [36-39] and three-dimensional (3D) elements [40, 41], just to name a few. On the other hand, it is also necessary to make great efforts to develop finite element models based on the CCST. Amongst the existing works, Darrall et al. [42] proposed the Lagrangian multiplier FE formulation for planar strain problems based on the CCST; Deng and Dargush [43, 44] developed a mixed Lagrangian multiplier formulation for elastodynamic and natural frequency analyses; Pedgaonkar et al. [45] also proposed a mixed FE formulation with primary variables of displacements and couple stresses for anisotropic centrosymmetric materials; Chakravarty et al. [46] developed the penalty-based finite element framework for the CCST; Poya et al. [47] proposed a family of numerical models for flexoelectricity continua and beam based on the CCST; Darrall et al. developed the 2D element formulation for mechanical-electric coupling in dielectrics [48]. In addition to the FEM, the boundary element method (BEM) has also been applied to the CCST [49-51]. However, the BEM is less popular than the FEM in practical engineering applications.

As discussed above, the C^1 continuity requirement may make the element performance highly susceptible to the mesh distortion. With the help of the Lagrangian multiplier method or penalty function method for enforcing the C^1 continuity requirement in weak sense, the distortion sensitivity problem can be alleviated to a certain extent, but not completely solved. The unsymmetric finite element method [52], that is fundamentally characterized by the usage of different interpolations respectively to design the test functions and trial functions of the element, emerged as a promising approach to develop distortion-immune elements. The first element developed based on the unsymmetric FEM is an 8-node membrane element whose stiffness matrix is unsymmetric [52]. But it should be pointed out that the unsymmetric FEM which belongs to the broad family of Petrov-Galerkin variational method does not necessarily yield unsymmetric element stiffness matrix. So far, the unsymmetric FEM has seen various successful applications in the classical continuum theory [53-58]. Recently, it has also been applied to the MCST through the developments of 4-node quadrilateral and 8-node hexahedral elements [59, 60]. The numerical experiments reveal that the elements can provide good predictions in analyzing the small-scale structures based on the MCST.

In the present work, the unsymmetric FEM is further applied to the CCST for verifying its effectiveness in simulating the size-dependent behaviors of consistent couple stress elasticity materials. By incorporating an independently assumed rotation field into the virtual work principle

and employing the penalty function method to consider the C^1 continuity requirement in weak sense, the penalty C^0 finite element framework is established. It is worth noticing that because the skew-symmetric part of stress in the CCST is essentially derived from the second derivatives of the rotation, its effects cannot be correctly predicted in terms of low-order 4-node quadrilateral element and 8-node hexahedral element. Therefore, only the 8-node quadrilateral element and 20-node hexahedral element are constructed within the proposed framework. In the new developments, the shape functions of the quadratic serendipity isoparametric elements are enriched by the nodal rotation degrees of freedom (DOFs) for determining the element test functions, whilst the stress functions that are derived from the concerned equilibrium equations are adopted as the basis functions for designing the trial functions. It is expected that the proposed new elements can also inherit the many advantages of the unsymmetric FEM when solving the consistent couple stress elastic problems, such as the good numerical accuracy in distorted meshes.

The rest of the paper is outlined below. In Section 2, we briefly introduce the basic equations of the CCST. In Section 3 and Section 4, the general formula of the penalty unsymmetric FEM and the detailed constructions of the new elements are provided respectively. The numerical examples are performed in Section 5 and the paper is concluded in Section 6.

2. Basic Equations of Consistent Couple Stress Elasticity

In this section, a brief description of the CCST [4] is presented. Considering a body subjected to a displacement field u_i, the strain ε_{ij} and mechanical rotation ω_i can be derived using the kinematical equations, respectively:

$$\varepsilon_{ij} = \frac{u_{i,j} + u_{j,i}}{2}, \quad \omega_i = \frac{1}{2} e_{ijk} u_{k,j} . \tag{1}$$

The mean curvature κ_{ij} which is defined as the skew-symmetric part of rotation gradient is given by

$$\kappa_{ij} = \frac{\omega_{i,j} - \omega_{j,i}}{2} . \tag{2}$$

The stress σ_{ij} in the CCST in general is non-symmetric and can be decomposed into the symmetric

part $\sigma_{(ij)}$ and the skew-symmetric part $\sigma_{[ij]}$:

$$\sigma_{ij} = \sigma_{(ij)} + \sigma_{[ij]}, \tag{3}$$

where only $\sigma_{(ij)}$ is the constitutive stress and work conjugates with the strain ε_{ij}, while $\sigma_{[ij]}$ has no contribution to the deformation energy. For the case of linear isotropic materials, the constitutive relations for $\sigma_{(ij)}$ may be written as

$$\sigma_{(ij)} = \lambda \varepsilon_{kk} \delta_{ij} + 2G\varepsilon_{ij}, \tag{4}$$

in which λ and G are the Lame's constants. Besides, the couple stress μ_{ij} which is the work conjugate pair of the mean curvature κ_{ij} is derived using the constitutive relations:

$$\mu_{ij} = -8Gl^2\kappa_{ij}, \tag{5}$$

in which l is the additional material length scale parameter for representing the size dependence of consistent couple stress elasticity material.

The equilibrium equations in the CCST are given by [4]

$$\sigma_{ji,j} + f_i = 0, \tag{6}$$

$$\mu_{ji,j} + e_{ijk}\sigma_{jk} = 0, \tag{7}$$

where f_i stands for the external body force. The external body couple load is not included because it can be transformed into an equivalent system of body forces and surface tractions [4]. By virtue of Equation (3), we can further obtain

$$\sigma_{(ji),j} + \sigma_{[ji],j} + f_i = 0, \tag{8}$$

$$\mu_{ji,j} + e_{ijk}\sigma_{[jk]} = 0, \tag{9}$$

from which one can clearly view that the skew-symmetric part of the stress $\sigma_{[jk]}$ are determined by the derivatives of the couple stress μ_{ij}.

In the CCST, the natural boundary conditions are given by [42]

$$\sigma_{ji}n_j = \bar{t}_i, \quad \mu_{ji}n_j = \bar{m}_i \tag{10}$$

in which $\bar{t}_i$ and $\bar{m}_i$ are the prescribed force traction and moment traction, respectively; n_j is the

6

cosine of the normal direction to the boundary. Besides, the essential boundary conditions take the form

$$u_i = \bar{u}_i, \quad \omega_i = \bar{\omega}_i \tag{11}$$

in which $\bar{u}_i$ and $\bar{\omega}_i$ are the prescribed displacement and rotation at the boundary.

For linear elastic materials obeying the CCST, the deformation energy density function is composed of two terms respectively generated by the strain and mean curvature:

$$U\left(\varepsilon_{ij}, \kappa_{ij}\right) = \frac{1}{2}\varepsilon_{ji}\sigma_{(ij)} + \frac{1}{2}\kappa_{ji}\mu_{ij} \tag{12}$$

3. General Formulation of Unsymmetric FEM

The derivation of the unsymmetric FEM directly begins from the virtual work principle [52]:

$$\delta\Pi = \delta\Pi_{in} - \delta\Pi_{ex} = 0 , \tag{13}$$

in which $\delta\Pi_{in}$ and $\delta\Pi_{ex}$ are the virtual works produced by the internal and external loads, respectively. For materials obeying the CCST, $\delta\Pi_{in}$ depends on the strain ε_{ij} and mean curvature κ_{ij} [4]:

$$\delta\Pi_{in} = \iint_{\Omega} \delta\varepsilon_{ji}\sigma_{(ij)}\mathrm{d}\Omega + \iint_{\Omega} \delta\kappa_{ji}\mu_{ij}\mathrm{d}\Omega , \tag{14}$$

while $\delta\Pi_{ex}$ takes the following form:

$$\delta\Pi_{ex} = \iint_{\Omega} \delta u_i f_i \mathrm{d}\Omega + \int_{\Gamma} \delta u_i R_i \mathrm{d}\Gamma + \int_{\Gamma} \delta\omega_i M_i \mathrm{d}\Gamma , \tag{15}$$

in which R_i and M_i are the external force and couple force applied to the boundary. In order to make the expressions more concise, they are rephrased in form of the vector and matrix based on the Voigt notation as follows:

$$\delta\Pi_{in} = \iint_{\Omega} \delta\boldsymbol{\varepsilon}(\mathbf{u})^{\mathrm{T}} \boldsymbol{\sigma}_{\mathrm{sym}}\mathrm{d}\Omega + \iint_{\Omega} \delta\boldsymbol{\kappa}(\mathbf{u})^{\mathrm{T}} \boldsymbol{\mu}\mathrm{d}\Omega , \tag{16}$$

$$\delta\Pi_{ex} = \iint_{\Omega} \delta\mathbf{u}^{\mathrm{T}}\mathbf{f}\mathrm{d}\Omega + \int_{\Gamma} \delta\mathbf{u}^{\mathrm{T}}\mathbf{R}\mathrm{d}\Gamma + \int_{\Gamma} \delta\boldsymbol{\omega}(\mathbf{u})^{\mathrm{T}} \mathbf{M}\mathrm{d}\Gamma . \tag{17}$$

For 2D/3D cases, the matrices and vectors in the preceding equations will have different concrete representations.

As shown in Equations (1) and (2), the mean curvatures in nature are the second-order derivatives of displacements. For ensuring the convergence, the straightforward FE implementation of Equation (13) will require the C^1 compatibility condition for the displacement interpolation, that is a very difficult task especially in the 3D case. To alleviate this problem, the curvatures can be derived from an independently assumed rotation field $\boldsymbol{\theta}$ instead of the mechanical rotation $\boldsymbol{\omega}$. The differences between these two rotation fields are eliminated by using the penalty function method [46]. Thereby, Equation (13) changes into

$$\delta\Pi^* = \delta\Pi_{in}^* - \delta\Pi_{ex}^* + k\iint_\Omega \delta\boldsymbol{\Lambda}^{\mathrm{T}}\boldsymbol{\Lambda}\mathrm{d}\Omega = 0 , \tag{18}$$

in which

$$\boldsymbol{\Lambda} = \boldsymbol{\theta} - \boldsymbol{\omega} , \tag{19}$$

and accordingly

$$\delta\Pi_{in}^* = \iint_\Omega \delta\boldsymbol{\varepsilon}(\mathbf{u})^{\mathrm{T}} \boldsymbol{\sigma}_{\mathrm{sym}}\mathrm{d}\Omega + \iint_\Omega \delta\boldsymbol{\kappa}(\boldsymbol{\theta})^{\mathrm{T}} \boldsymbol{\mu}\mathrm{d}\Omega , \tag{20}$$

$$\delta\Pi_{ex}^* = \iint_\Omega \delta\mathbf{u}^{\mathrm{T}}\mathbf{f}\mathrm{d}\Omega + \int_\Gamma \delta\mathbf{u}^{\mathrm{T}}\mathbf{R}\mathrm{d}\Gamma + \int_\Gamma \delta\boldsymbol{\theta}^{\mathrm{T}}\mathbf{M}\mathrm{d}\Gamma . \tag{21}$$

k is the penalty parameter that should be chosen carefully to enforce the constraint satisfied in the accept level and not to make the condition number of the finally stiffness matrix overly large.

As discussed above, the unsymmetric FEM is characteristic of designing the element's test function and trial function using different interpolations. In general, both the test function and trial function in FEM can be ultimately expressed in terms of the element nodal DOF vector $\mathbf{q}^e$. With regard to the present elements, the test functions of the displacement and rotation which are separately constructed have the expressions:

$$\mathbf{u} = \bar{\mathbf{u}} = \bar{\mathbf{N}}\mathbf{q}^e , \tag{22}$$

$$\boldsymbol{\theta} = \bar{\boldsymbol{\theta}} = \bar{\mathbf{N}}^\theta\mathbf{q}^e , \tag{23}$$

which lead to the strain and mean curvature by virtue of Equations (1) and (2):

$$\boldsymbol{\varepsilon} = \bar{\boldsymbol{\varepsilon}}(\bar{\mathbf{u}}) = \bar{\mathbf{B}}^n\mathbf{q}^e , \tag{24}$$

$$\boldsymbol{\kappa} = \bar{\boldsymbol{\kappa}}(\bar{\boldsymbol{\theta}}) = \bar{\mathbf{B}}^c\mathbf{q}^e ; \tag{25}$$

meanwhile, the trial functions of the work-conjugated stress and couple stress are

$$\boldsymbol{\sigma}_{\mathrm{sym}} = \hat{\boldsymbol{\sigma}}_{\mathrm{sym}} = \hat{\mathbf{S}}^n\mathbf{q}^e , \tag{26}$$

$$\boldsymbol{\mu} = \hat{\boldsymbol{\mu}} = \hat{\mathbf{S}}^c \mathbf{q}^e . \tag{27}$$

Besides, the matrix $\boldsymbol{\Lambda}$ takes the form:

$$\boldsymbol{\Lambda} = \overline{\boldsymbol{\theta}} - \overline{\boldsymbol{\omega}}(\overline{\mathbf{u}}) = \overline{\mathbf{N}}^{\Lambda} \mathbf{q}^e . \tag{28}$$

By inserting the foregoing definitions back into Equation (18) and applying the virtual work principle, the final equation to be solved is derived as

$$\mathbf{K}^e \mathbf{q}^e = \mathbf{P}^e , \tag{29}$$

in which $\mathbf{K}^e$ is the stiffness matrix

$$\mathbf{K}^e = \iint_{\Omega} \overline{\mathbf{B}}^{n\mathrm{T}} \hat{\mathbf{S}}^n \mathrm{d}\Omega + \iint_{\Omega} \overline{\mathbf{B}}^{c\mathrm{T}} \hat{\mathbf{S}}^c \mathrm{d}\Omega + k \iint_{\Omega} \overline{\mathbf{N}}^{\Lambda\mathrm{T}} \overline{\mathbf{N}}^{\Lambda} \mathrm{d}\Omega , \tag{30}$$

and $\mathbf{P}^e$ is the equivalent nodal load vector

$$\mathbf{P}^e = \iint_{\Omega} \overline{\mathbf{N}}^{\mathrm{T}} \mathbf{f} \mathrm{d}\Omega + \int_{\Gamma} \overline{\mathbf{N}}^{\mathrm{T}} \mathbf{R} \mathrm{d}\Gamma + \int_{\Gamma} \overline{\mathbf{N}}^{\theta\mathrm{T}} \mathbf{M} \mathrm{d}\Gamma . \tag{31}$$

Within the newly established unsymmetric FE framework, different 2D and 3D elements can be developed. However, considering that the skew-symmetric part of stress in the CCST is essentially the second derivatives of the rotation as shown in Equations (5) and (9), which cannot be correctly reproduced by the low-order 4-node quadrilateral elements and 8-node hexahedral elements, only the 8-node 2D quadrilateral element and 20-node 3D hexahedral element are developed in this work. Their detailed construction procedures are discussed in the next section.

4. New Elements for CCST

4.1. The 8-node quadrilateral element for CCST

Let us consider an 8-node quadrilateral element that has two translation DOFs and one rotation DOF per node for the 2D consistent couple stress problems, as shown in Figure 1, the element nodal DOF vector $\mathbf{q}^e$ is described as

$$\mathbf{q}^e = \begin{bmatrix} \mathbf{q}_1^e & \mathbf{q}_2^e & \mathbf{q}_3^e & \cdots & \mathbf{q}_8^e \end{bmatrix}^{\mathrm{T}} , \tag{32}$$

with

$$\mathbf{q}_i^e = \begin{bmatrix} u_i & v_i & \theta_{zi} \end{bmatrix} , \quad i = 1 \sim 8 . \tag{33}$$

As previously discussed, C^0 continuous interpolations can be used for designing the test functions

of the displacement within the present penalty FE framework. The commonly used C^0 quadratic serendipity isoparametric shape function seems like an obvious choice. But it has been proved that its performance is not as satisfactory as expected in the couple stress elasticity problems [61]. For the 3-node triangular and 4-node quadrilateral elements, the famous Allman's interpolation [62, 63] is a very important technique to use the drilling DOFs to enrich the displacement field. However, the original version of the Allman's interpolation is only the boundary interpolation, and the scheme is very tedious when it is directly extended to in-domain interpolation. Shang and Ouyang [64] proposed an interpolation for 4-node quadrilateral element that has a relatively concise expression and coincides with the standard Allman's interpolation along the element boundary. Recently, this kind of interpolation has been applied to the elements based on the couple stress theories [59, 60]. In this work, the standard 8-node isoparametric interpolation is enriched by the nodal rotation DOFs through the above-mentioned approach and accordingly, the matrices $\bar{\mathbf{u}}$ and $\bar{\mathbf{N}}$ in Equation (22) are presented as

$$\bar{\mathbf{u}} = \left\{ \begin{array}{c} \bar{u} \\ \bar{v} \end{array} \right\} = \bar{\mathbf{N}} \mathbf{q}^e, \quad \bar{\mathbf{N}} = \begin{bmatrix} \bar{\mathbf{N}}_1 & \bar{\mathbf{N}}_2 & \cdots & \bar{\mathbf{N}}_8 \end{bmatrix}, \tag{34}$$

with

$$\bar{\mathbf{N}}_i = \begin{bmatrix} N_i & 0 & -\dfrac{1}{2} N_i \left(y - y_i \right) \\ 0 & N_i & \dfrac{1}{2} N_i \left(x - x_i \right) \end{bmatrix}, \quad i = 1 \sim 8, \tag{35}$$

in which $\left(x_i, y_i \right)$ are the Cartesian coordinates of the node i; N_i is the standard isoparametric shape function of the 8-node quadrilateral element:

$$N_i = \begin{cases} -\dfrac{1}{4}\left(1+\xi_i\xi\right)\left(1+\eta_i\eta\right)\left(1-\xi_i\xi-\eta_i\eta\right) & \left(i=1\sim4\right) \\ \dfrac{1}{2}\left(1-\xi^2\right)\left(1+\eta_i\eta\right) & \left(i=5,7\right), \\ \dfrac{1}{2}\left(1-\eta^2\right)\left(1+\xi_i\xi\right) & \left(i=6,8\right) \end{cases} \tag{36}$$

At the same time, the rotation in Equation (23) is determined by

$$\bar{\boldsymbol{\theta}} = \left\{ \bar{\theta}_z \right\} = \bar{\mathbf{N}}^\theta \mathbf{q}^e, \quad \bar{\mathbf{N}}^\theta = \begin{bmatrix} \bar{\mathbf{N}}_1^\theta & \bar{\mathbf{N}}_2^\theta & \cdots & \bar{\mathbf{N}}_8^\theta \end{bmatrix}, \tag{37}$$

with

$$\bar{\mathbf{N}}_i^\theta = \begin{bmatrix} 0 & 0 & N_i \end{bmatrix}, \quad i = 1 \sim 8; \tag{38}$$

and accordingly, the detailed expression of Equation (28) is obtained:

$$\Lambda = \left\{ \bar{\theta}_z - \frac{1}{2}\left(\frac{\partial \bar{v}}{\partial x} - \frac{\partial \bar{u}}{\partial y} \right) \right\} = \bar{\mathbf{N}}^\Lambda \mathbf{q}^e, \quad \bar{\mathbf{N}}^\Lambda = \begin{bmatrix} \bar{\mathbf{N}}_1^\Lambda & \bar{\mathbf{N}}_2^\Lambda & \cdots & \bar{\mathbf{N}}_8^\Lambda \end{bmatrix}, \tag{39}$$

in which the submatrices $\bar{\mathbf{N}}_i^\Lambda$ is given by

$$\bar{\mathbf{N}}_i^\Lambda = \frac{1}{2}\left[-N_{i,y} \quad N_{i,x} \quad \frac{1}{2}N_{i,x}(x - x_i) + \frac{1}{2}N_{i,y}(y - y_i) - N_i \right], \quad i = 1 \sim 8. \tag{40}$$

Subsequently, the test functions of the strain and curvature in Equations (24) and (25) are delivered, respectively:

$$\bar{\boldsymbol{\varepsilon}} = \left\{ \begin{array}{c} \bar{\varepsilon}_{xx} \\ \bar{\varepsilon}_{yy} \\ 2\bar{\varepsilon}_{xy} \end{array} \right\} = \bar{\mathbf{B}}^n \mathbf{q}^e, \quad \bar{\mathbf{B}}^n = \begin{bmatrix} \bar{\mathbf{B}}_1^n & \bar{\mathbf{B}}_2^n & \cdots & \bar{\mathbf{B}}_8^n \end{bmatrix}, \tag{41}$$

$$\bar{\boldsymbol{\kappa}} = \left\{ \begin{array}{c} 2\bar{\kappa}_{zx} \\ 2\bar{\kappa}_{zy} \end{array} \right\} = \left\{ \begin{array}{c} -2\bar{\kappa}_{xz} \\ -2\bar{\kappa}_{yz} \end{array} \right\} = \bar{\mathbf{B}}^c \mathbf{q}^e, \quad \bar{\mathbf{B}}^c = \begin{bmatrix} \bar{\mathbf{B}}_1^c & \bar{\mathbf{B}}_2^c & \cdots & \bar{\mathbf{B}}_8^c \end{bmatrix}, \tag{42}$$

in which

$$\bar{\mathbf{B}}_i^n = \begin{bmatrix} N_{i,x} & 0 & -\frac{1}{2}N_{i,x}(y - y_i) \\ 0 & N_{i,y} & \frac{1}{2}N_{i,y}(x - x_i) \\ N_{i,y} & N_{i,x} & \frac{1}{2}N_{i,x}(x - x_i) - \frac{1}{2}N_{i,y}(y - y_i) \end{bmatrix}, \quad i = 1 \sim 8, \tag{43}$$

$$\bar{\mathbf{B}}_i^c = \begin{bmatrix} 0 & 0 & N_{i,x} \\ 0 & 0 & N_{i,y} \end{bmatrix}, \quad i = 1 \sim 8. \tag{44}$$

On the other hand, as promised before, the trial functions of stress and couple stress are formulated based on the stress functions that can satisfy the equilibrium equations of the problem of interest. Thus, these stress functions should be first derived. The equilibrium equations in the 2D consistent couple stress elasticity problems are derived by substituting Equation (9) into Equation (8), as follows:

$$\begin{cases} \dfrac{\partial \sigma_{(xx)}}{\partial x} + \dfrac{\partial \sigma_{(yx)}}{\partial y} + \dfrac{1}{2}\dfrac{\partial^2 \mu_{yz}}{\partial y^2} + \dfrac{1}{2}\dfrac{\partial^2 \mu_{xz}}{\partial x \partial y} + f_x = 0 \\ \dfrac{\partial \sigma_{(xy)}}{\partial x} + \dfrac{\partial \sigma_{(yy)}}{\partial y} - \dfrac{1}{2}\dfrac{\partial^2 \mu_{yz}}{\partial x \partial y} - \dfrac{1}{2}\dfrac{\partial^2 \mu_{xz}}{\partial x^2} + f_y = 0 \end{cases}. \tag{45}$$

The solutions of above the differential equation system are comprised of the homogeneous part and

particular part. The existence of body force means that the particular solution part is not zero. In view of the fact that the external body forces are considered in the finite element model in the form of equivalent nodal loads ultimately, the particular solution can be omitted for sake of simplicity. This simplification will bring some error, but the error decreases with the mesh refinement. Herein, only the homogeneous part is concerned which should satisfy

$$\begin{cases} \dfrac{\partial \sigma_{(xx)}}{\partial x} + \dfrac{\partial \sigma_{(yx)}}{\partial y} + \dfrac{1}{2}\dfrac{\partial^2 \mu_{yz}}{\partial y^2} + \dfrac{1}{2}\dfrac{\partial^2 \mu_{xz}}{\partial x \partial y} = 0 \\ \dfrac{\partial \sigma_{(xy)}}{\partial x} + \dfrac{\partial \sigma_{(yy)}}{\partial y} - \dfrac{1}{2}\dfrac{\partial^2 \mu_{yz}}{\partial x \partial y} - \dfrac{1}{2}\dfrac{\partial^2 \mu_{xz}}{\partial x^2} = 0 \end{cases}. \tag{46}$$

Since it is very difficult and tedious to simultaneously derive the desired stress and couple stress functions by solving Equation (46), we make the following simplification: splitting Equation (46) into two parts and solving them separately:

$$\begin{cases} \dfrac{\partial \sigma_{(xx)}}{\partial x} + \dfrac{\partial \sigma_{(yx)}}{\partial y} = 0 \\ \dfrac{\partial \sigma_{(xy)}}{\partial x} + \dfrac{\partial \sigma_{(yy)}}{\partial y} = 0 \end{cases}, \tag{47}$$

and

$$\begin{cases} \dfrac{1}{2}\dfrac{\partial^2 \mu_{yz}}{\partial y^2} + \dfrac{1}{2}\dfrac{\partial^2 \mu_{xz}}{\partial x \partial y} = 0 \\ -\dfrac{1}{2}\dfrac{\partial^2 \mu_{yz}}{\partial x \partial y} - \dfrac{1}{2}\dfrac{\partial^2 \mu_{xz}}{\partial x^2} = 0 \end{cases}. \tag{48}$$

It is worth noticing that, the stress and couple stress functions obtained by this approach is only a subset of that of Equation (46). Although the difficulty of derivation is reduced, this approach gives rise to a certain approximation. Thus, its validness and effectiveness should be carefully checked by the numerical tests.

One can observe that Equation (47) has exactly the same form with the ones of the 2D classical continuum elasticity. This means the existing Airy stress solutions in the classical continuum elasticity [65] provide a potential choice to be the basic functions for designing the symmetric part of the stress in the CCST. Thereby, $\hat{\boldsymbol{\sigma}}_{\text{sym}}$ in Equation (26) can be initially described as

$$\hat{\boldsymbol{\sigma}}_{\text{sym}} = \begin{Bmatrix} \hat{\sigma}_{(xx)} \\ \hat{\sigma}_{(yy)} \\ \hat{\sigma}_{(xy)} \end{Bmatrix} = \mathbf{H}^n \boldsymbol{\alpha}, \tag{49}$$

with

$$\boldsymbol{\alpha} = \begin{bmatrix} \alpha_1 & \alpha_2 & ... & \alpha_{15} \end{bmatrix}^{\text{T}}, \tag{50}$$

in which $\mathbf{H}^n$ is composed of the Airy stress solutions which are summarized in Table 1. Next, for rewriting $\hat{\boldsymbol{\sigma}}_{\text{sym}}$ in terms of the nodal DOF vector $\mathbf{q}^e$, the coming weighted residual condition which means that the work done by the two different strains is equal to each other for the given stress state is considered:

$$\iint_{\Omega} \mathbf{M} \left(\bar{\boldsymbol{\varepsilon}} - \mathbf{D}_n^{-1} \hat{\boldsymbol{\sigma}}_{\text{sym}} \right) t \, \mathrm{d}\Omega = \mathbf{0}, \tag{51}$$

in which the weight function matrix $\mathbf{M}$ is simply set as $\mathbf{H}^{n\text{T}}$; under plane strain assumption, $\mathbf{D}_n$ is given by

$$\mathbf{D}_n = \frac{E}{(1+v)(1-2v)} \begin{bmatrix} 1-v & v & 0 \\ v & 1-v & 0 \\ 0 & 0 & (1-2v)/2 \end{bmatrix}, \tag{52}$$

where E and v are the Young's modulus and Poisson's ratio. Note that only the plain strain state is considered here because the plane stress state cannot be exactly reduced to a two-dimensional problem in the couple stress theory. Using Equation (41) and Equation (49), Equation (51) leads to

$$\mathbf{V}_n \mathbf{q}^e = \mathbf{M}_n \boldsymbol{\alpha}, \tag{53}$$

with

$$\mathbf{V}_n = \iint_{\Omega} \mathbf{H}^{n\text{T}} \bar{\mathbf{B}}^n t \, \mathrm{d}\Omega, \quad \mathbf{M}_n = \iint_{\Omega} \mathbf{H}^{n\text{T}} \mathbf{D}_n^{-1} \mathbf{H}^n t \, \mathrm{d}\Omega, \tag{54}$$

from which we can obtain

$$\boldsymbol{\alpha} = \mathbf{M}_n^{-1} \mathbf{V}_n \mathbf{q}^e, \tag{55}$$

Ultimately, the required expression of $\hat{\boldsymbol{\sigma}}_{\text{sym}}$ is deduced by inserting Equation (55) back into Equation (49):

$$\hat{\boldsymbol{\sigma}}_{\text{sym}} = \hat{\mathbf{S}}^n \mathbf{q}^e, \quad \hat{\mathbf{S}}^n = \mathbf{H}^n \mathbf{M}_n^{-1} \mathbf{V}_n. \tag{56}$$

Analogously, the couple stress $\hat{\boldsymbol{\mu}}$ can initially take the following form that can satisfy Equation

(48):

$$\hat{\boldsymbol{\mu}} = \mathbf{H}^c \boldsymbol{\beta}, \tag{57}$$

in which

$$\mathbf{H}^c = \begin{bmatrix} 1 & 0 & x & 0 & y & 0 & x^2 & 0 & y^2 & -2xy \\ 0 & 1 & 0 & x & 0 & y & -2xy & x^2 & 0 & y^2 \end{bmatrix}, \tag{58}$$

$$\boldsymbol{\beta} = \begin{bmatrix} \beta_1 & \beta_2 & \cdots & \beta_{10} \end{bmatrix}^{\mathrm{T}}. \tag{59}$$

By following the same path outlined in Equation (51), the relation between $\boldsymbol{\beta}$ and $\mathbf{q}^e$ can be obtained:

$$\boldsymbol{\beta} = \mathbf{M}_c^{-1} \mathbf{V}_c \mathbf{q}^e, \tag{60}$$

with

$$\mathbf{M}_c = \iint_\Omega \mathbf{H}^{c\mathrm{T}} \mathbf{D}_c^{-1} \mathbf{H}^c t \mathrm{d}\Omega, \quad \mathbf{V}_c = \iint_\Omega \mathbf{H}^{c\mathrm{T}} \bar{\mathbf{B}}^c t \mathrm{d}\Omega. \tag{61}$$

in which $\bar{\mathbf{B}}^c$ is given by Equation (42) and

$$\mathbf{D}_c = \begin{bmatrix} 4Gl^2 & 0 \\ 0 & 4Gl^2 \end{bmatrix}. \tag{62}$$

Finally, the following expression is deduced by inserting Equation (60) back into Equation (57):

$$\hat{\boldsymbol{\mu}} = \hat{\mathbf{S}}^c \mathbf{q}^e, \quad \hat{\mathbf{S}}^c = \mathbf{H}^c \mathbf{M}_c^{-1} \mathbf{V}_c. \tag{63}$$

Note that the material length scale parameter l appears in the denominator in the process of matrix inversion shown in Equation (61). Thus, when dealing with the cases where l is very small, it is necessary to use the floating-point number type with sufficient precision in finite element programming for ensuring the accuracy of numerical calculation.

As the detailed expressions of the test functions and trial functions of the new 8-node quadrilateral element have been determined, the element stiffness matrix and equivalent nodal load vector can be calculated in accordance with Equations (30) and (31). After $\mathbf{q}^e$ being solved, the symmetric part of the stress and the couple stress can be respectively calculated using Equations (56) and (63), whilst the skew-symmetric part of the stress is derived by further substituting the obtained couple stress into Equation (9).

It is noted that, even though the locking problem experienced by the penalty stiffness [66] is not

as serious as the 4-node lower order element, the 1×1 reduced quadrature scheme is suggested for calculating the penalty stiffness for purpose of further improving the element performance without resulting in spurious zero energy modes. Moreover, it can be easily proved that when all the integrals except the penalty stiffness are evaluated using the full quadrature scheme, the stiffness matrix of the new element is symmetric. In other words, if the reduced quadrature scheme is used in part of the integrals, the unsymmetric element stiffness matrix will be obtained. For instance, the one-point quadrature strategy is used to calculated the final stiffness integral in [67] for enhancing the element behavior and the resulted element stiffness matrix is unsymmetric. The findings reveal that the unsymmetric FEM which essentially belongs to the broad family of the Petrov-Galerkin (PG) variational method, does not necessarily yield unsymmetric element stiffness matrix, although the test and trial functions are constructed using different interpolations. Actually, it has already be reported that it is possible to derive the preferred symmetric linear equations from PG variational with some specific processing [68, 69]. It may provide a promising approach to overcome the computation inefficiency problem caused by the stiffness matrix's unsymmetry while retaining many advantages of the original unsymmetric FEM.

4.2. The 20-node hexahedral element for CCST

The 20-node hexahedral element for the 3D consistent couple stress problems can be constructed in the same way. As shown in Figure 2, the developed hexahedral element has three translation DOFs and three rotation DOFs per node. The element nodal DOF vector $\mathbf{q}^e$ is

$$\mathbf{q}^e = \begin{bmatrix} \mathbf{q}_1^e & \mathbf{q}_2^e & \mathbf{q}_3^e & \cdots & \mathbf{q}_{20}^e \end{bmatrix}^{\mathrm{T}}, \tag{64}$$

with

$$\mathbf{q}_i^e = \begin{bmatrix} u_i & v_i & w_i & \theta_{xi} & \theta_{yi} & \theta_{zi} \end{bmatrix}, \quad i = 1 \sim 20. \tag{65}$$

The test function of the displacement is formulated in the same way as the 2D case in that the displacement is enhanced by the nodal rotation DOFs:

$$\bar{\mathbf{u}} = \begin{Bmatrix} \bar{u} \\ \bar{v} \\ \bar{w} \end{Bmatrix} = \bar{\mathbf{N}} \mathbf{q}^e, \quad \bar{\mathbf{N}} = \begin{bmatrix} \bar{\mathbf{N}}_1 & \bar{\mathbf{N}}_2 & \cdots & \bar{\mathbf{N}}_{20} \end{bmatrix}, \tag{66}$$

with

$$\bar{\mathbf{N}}_i = \begin{bmatrix} N_i & 0 & 0 & 0 & \frac{1}{2}N_i(z-z_i) & -\frac{1}{2}N_i(y-y_i) \\ 0 & N_i & 0 & -\frac{1}{2}N_i(z-z_i) & 0 & \frac{1}{2}N_i(x-x_i) \\ 0 & 0 & N_i & \frac{1}{2}N_i(y-y_i) & -\frac{1}{2}N_i(x-x_i) & 0 \end{bmatrix}, \quad i=1\sim 20, \quad (67)$$

in which N_i is the standard isoparametric shape function of the 20-node hexahedral element

$$N_i = \begin{cases} \frac{1}{8}(1+\xi_i\xi)(1+\eta_i\eta)(1+\zeta_i\zeta)(-2+\xi_i\xi+\eta_i\eta+\zeta_i\zeta) & (i=1\sim 8) \\ \frac{1}{4}(1-\xi^2)(1+\eta_i\eta)(1+\zeta_i\zeta) & (i=9,11,13,15) \\ \frac{1}{4}(1-\eta^2)(1+\xi_i\xi)(1+\zeta_i\zeta) & (i=10,12,14,16) \\ \frac{1}{4}(1-\zeta^2)(1+\xi_i\xi)(1+\eta_i\eta) & (i=17,18,19,20) \end{cases}, \quad (68)$$

Besides, the rotation in Equation (23) takes the interpolation

$$\bar{\mathbf{\theta}} = \begin{Bmatrix} \bar{\theta}_x \\ \bar{\theta}_y \\ \bar{\theta}_z \end{Bmatrix} = \bar{\mathbf{N}}^\theta \mathbf{q}^e, \quad \bar{\mathbf{N}}^\theta = \begin{bmatrix} \bar{\mathbf{N}}_1^\theta & \bar{\mathbf{N}}_2^\theta & \cdots & \bar{\mathbf{N}}_{20}^\theta \end{bmatrix}, \quad (69)$$

where the submatrices in $\bar{\mathbf{N}}^\theta$ read

$$\bar{\mathbf{N}}_i^\theta = \begin{bmatrix} 0 & 0 & 0 & N_i & 0 & 0 \\ 0 & 0 & 0 & 0 & N_i & 0 \\ 0 & 0 & 0 & 0 & 0 & N_i \end{bmatrix}, \quad i=1\sim 20. \quad (70)$$

Accordingly, the expression of Equation (28) is

$$\mathbf{\Lambda} = \begin{Bmatrix} \bar{\theta}_x - \frac{1}{2}\left(\frac{\partial \bar{w}}{\partial y} - \frac{\partial \bar{v}}{\partial z}\right) \\ \bar{\theta}_y - \frac{1}{2}\left(\frac{\partial \bar{u}}{\partial z} - \frac{\partial \bar{w}}{\partial x}\right) \\ \bar{\theta}_z - \frac{1}{2}\left(\frac{\partial \bar{v}}{\partial x} - \frac{\partial \bar{u}}{\partial y}\right) \end{Bmatrix} = \bar{\mathbf{N}}^\Lambda \mathbf{q}^e, \quad \bar{\mathbf{N}}^\Lambda = \begin{bmatrix} \bar{\mathbf{N}}_1^\Lambda & \bar{\mathbf{N}}_2^\Lambda & \cdots & \bar{\mathbf{N}}_{20}^\Lambda \end{bmatrix}, \quad (71)$$

in which

$$\bar{\mathbf{N}}_i^\Lambda = \begin{bmatrix} \bar{\mathbf{N}}_{\alpha i}^\Lambda & \bar{\mathbf{N}}_{\beta i}^\Lambda \end{bmatrix}, \quad i=1\sim 20, \quad (72)$$

with

$$\bar{\mathbf{N}}_{\alpha i}^\Lambda = \frac{1}{2}\begin{bmatrix} 0 & -N_{i,z} & N_{i,y} \\ N_{i,z} & 0 & -N_{i,x} \\ -N_{i,y} & N_{i,x} & 0 \end{bmatrix}, \quad (73)$$

16

$$\bar{\mathbf{N}}_{\beta i}^{\Lambda} = \frac{1}{4}\begin{bmatrix} N_{i,z}(z-z_i)+N_{i,y}(y-y_i)-2N_i & -N_{i,y}(x-x_i) & -N_{i,z}(x-x_i) \\ -N_{i,x}(y-y_i) & N_{i,z}(z-z_i)+N_{i,x}(x-x_i)-2N_i & -N_{i,z}(y-y_i) \\ -N_{i,x}(z-z_i) & -N_{i,y}(z-z_i) & N_{i,y}(y-y_i)+N_{i,x}(x-x_i)-2N_i \end{bmatrix}.$$

(74)

The corresponding test functions of the strain and curvature are respectively determined by:

$$\bar{\boldsymbol{\varepsilon}} = \begin{Bmatrix} \bar{\varepsilon}_{xx} \\ \bar{\varepsilon}_{yy} \\ \bar{\varepsilon}_{zz} \\ 2\bar{\varepsilon}_{xy} \\ 2\bar{\varepsilon}_{yz} \\ 2\bar{\varepsilon}_{xz} \end{Bmatrix} = \bar{\mathbf{B}}^n \mathbf{q}^e, \quad \bar{\mathbf{B}}^n = \begin{bmatrix} \bar{\mathbf{B}}_1^n & \bar{\mathbf{B}}_2^n & \dots & \bar{\mathbf{B}}_{20}^n \end{bmatrix},$$

(75)

$$\bar{\boldsymbol{\kappa}} = \begin{Bmatrix} 2\bar{\kappa}_{yx} \\ 2\bar{\kappa}_{zy} \\ 2\bar{\kappa}_{zx} \end{Bmatrix} = \begin{Bmatrix} -2\bar{\kappa}_{xy} \\ -2\bar{\kappa}_{yz} \\ -2\bar{\kappa}_{xz} \end{Bmatrix} = \bar{\mathbf{B}}^c \mathbf{q}^e, \quad \bar{\mathbf{B}}^c = \begin{bmatrix} \bar{\mathbf{B}}_1^c & \bar{\mathbf{B}}_2^c & \dots & \bar{\mathbf{B}}_{20}^c \end{bmatrix}.$$

(76)

Upon substitutions of Equations (66) and (69) into the kinematical relationships, the detailed constituents of the matrices $\bar{\mathbf{B}}^n$ and $\bar{\mathbf{B}}^c$ in above equations can be evaluated.

Similar with the quadrilateral element, the trial functions of stress and couple stress of the present 20-node hexahedral element are firstly designed based on the stress functions which can satisfy the 3D equilibrium Equations (8) and (9), as follows:

$$\hat{\boldsymbol{\sigma}}_{\text{sym}} = \begin{Bmatrix} \hat{\sigma}_{(xx)} \\ \hat{\sigma}_{(yy)} \\ \hat{\sigma}_{(zz)} \\ \hat{\sigma}_{(xy)} \\ \hat{\sigma}_{(yz)} \\ \hat{\sigma}_{(xz)} \end{Bmatrix} = \mathbf{H}^n \boldsymbol{\alpha}, \quad \hat{\boldsymbol{\mu}} = \begin{Bmatrix} \hat{\mu}_{xy} \\ \hat{\mu}_{yz} \\ \hat{\mu}_{xz} \end{Bmatrix} = \mathbf{H}^c \boldsymbol{\beta}.$$

(77)

Using the same simplification with the 2D case, the desired stress and couple stress functions for the 3D problem can be derived. For the sake of simplicity, the detailed components of the matrices $\mathbf{H}^n$ and $\mathbf{H}^c$ are summarized in Tables 2 and 3. It is worthy noticing that the above assumed stress and couple stress fields can satisfy the homogeneous parts of the concerned three-dimensional equilibrium equations. In accordance with the matrices $\mathbf{H}^n$ and $\mathbf{H}^c$ in Equation (77), $\boldsymbol{\alpha}$ and $\boldsymbol{\beta}$ respectively are:

$$\boldsymbol{\alpha} = \begin{bmatrix} \alpha_1 & \alpha_2 & \dots & \alpha_{48} \end{bmatrix}^{\mathrm{T}},$$

(78)

$$\boldsymbol{\beta} = \begin{bmatrix} \beta_1 & \beta_2 & \cdots & \beta_{27} \end{bmatrix}^{\mathrm{T}}. \tag{79}$$

Next, by following the same process in Section 4.1, the above stress and couple stress can be rewritten in terms of the element nodal DOF vector $\mathbf{q}^e$.

The detailed formulation of the new 20-node hexahedral element can be finally established through the substitutions of the above test functions and trial functions back into Equations (30) and (31). It is noted that the reduced 3×3×3 quadrature strategy which herein doesn't lead to spurious zero energy modes is suggested for evaluating the penalty stiffness contribution.

5. Numerical Validations

For purpose of adequately assessing the validities of the new 8-node quadrilateral and 20-node hexahedral elements in predicting the size-dependent mechanical responses of consistent couple stress elasticity materials, a series of benchmark examples are investigated. The solutions obtained using either the analytical method or other numerical approaches are also provided as the reference values for comprehensive comparison. In these tests, the penalty parameter is set as $k/G = 10^4$ that has been demonstrated by parametric analysis to be a prober value in practical applications.

5.1. Tests for 2D consistent couple stress elasticity

5.1.1 The 2D patch test

As suggested by [70], the $C^{0\text{-}1}$ patch test is used for examining whether the new quadrilateral element based on the CCST satisfies the convergence criterion. Figure 3 shows the typical meshes in which Mesh b and Mesh c contain heavily distorted element in the shape of degenerated triangle or concave quadrangle. The displacements and rotations calculated at the boundary nodes in accordance with the following functions are applied to the patch as the prescribed boundary conditions:

$$u = a_1 + a_2 x + a_3 y + a_4 x^2 - 2\left[(1-2v)b_4 + 2(1-v)b_5\right]xy + a_5 y^2, \tag{80}$$

$$v = b_1 + b_2 x + b_3 y + b_4 x^2 - 2\left[2(1-v)a_4 + (1-2v)a_5\right]xy + b_5 y^2, \tag{81}$$

$$2\omega_z = b_2 + 2b_4 x - 2\left[2(1-v)a_4 + (1-2v)a_5\right]y - a_3 - 2a_5 y + 2\left[(1-2v)b_4 + 2(1-v)b_5\right]x, \tag{82}$$

in which the coefficients are listed in Table 4. The results at the inner nodes are monitored. The numerical results show that the new element can always accurately reproduce the constant stress state and constant couple stress state no matter what badly distorted meshes are used, demonstrating that the computation convergence of the new quadrilateral element is guaranteed.

5.1.2 Deformation of the circular ring

As illustrated in Figure 4, the circular ring is fully fixed at the outer periphery while the prescribed boundary conditions at its internal surface are set as [46]

$$u_\theta = 1\text{mm}, \quad u_r = 0. \tag{83}$$

Three different ratios of the material length scale parameter to the inner radius (l/a=0.25, 0.5, 1) are considered. The computations are operated by dividing the ring into $M \times N$ elements, in which M and N respectively denote the element numbers in the circumferential direction and radial direction. As is evident in Table 5 that, the numerical results converge into the reference solutions [46] very rapidly. Moreover, the distributions of the tangential displacement u_θ, the rotation ω_z, the symmetric part of shear stress $\sigma_{(r\theta)}$ and the couple stress μ_{rz} along the radial path AB calculated by using 64×16 elements are provided in Figure 5. One can clearly observe that the numerical values are in good agreements with the reference ones. It's noted that the present FE results can not exactly satisfy the zero-value stress boundary condition but the errors can be gradually eliminated with the mesh refinement.

5.1.3 The plate with a hole

As shown in Figure 6, the square plate with a central circular hole under uniform uniaxial tension is investigated to study the size effect. Due to symmetry, only a quarter of the plate is modeled by using the typical meshes as depicted in Figure 7. The convergence results of the nominal stress concentration factors for different material length scale parameters are summarized in Table 6 and the horizontal displacements respectively calculated at the points B and C are listed in Table 7. Because there are no analytical solutions available in the open literature, the results delivered by the boundary element method [49] are provided here as the reference values. It is obvious that with the increase of the material length scale parameter, the stress concentration is gradually reduced,

indicating that the curvatures have an increasing contribution to the deformation energy.

5.1.4 The simple shear problem

As shown in Figure 8, to model an infinite stripe subjected to simple shear boundary conditions, the slender rectangle which is clamped at its bottom is considered. At the top surface, the vertical displacement and rotation are constrained and the horizontal displacement is prescribed as $U=1\mu m$. The variations of the horizontal displacement and rotation along the y-axis are evaluated. As discussed in [15], the solutions of this simple shear problem based on the CCST coincide with that of the MSCT. Thereby, the analytical solutions can be simply derived from the ones originally proposed for MSCT [71] by replacing the corresponding material length scale parameter:

$$u(y) = C_1 + C_2 y + C_3 e^{\alpha y} + C_4 e^{-\alpha y}, \tag{84}$$

$$\omega_z(y) = -\frac{1}{2}\left(C_2 + C_3 \alpha e^{\alpha y} - C_4 \alpha e^{-\alpha y}\right), \tag{85}$$

in which

$$C_1 = \beta\left(e^{-\alpha h} + e^{\alpha h} - 2\right), \quad C_2 = \beta\left(e^{-\alpha h} - e^{\alpha h}\right)\big/l, \quad C_3 = \beta\left(1 - e^{-\alpha h}\right), \quad C_4 = \beta\left(1 - e^{\alpha h}\right), \tag{86}$$

with

$$\alpha = \frac{1}{l}, \quad 2\beta = \frac{U}{-2 + \left(1 + \alpha h/2\right)e^{-\alpha h} + \left(1 - \alpha h/2\right)e^{\alpha h}}. \tag{87}$$

In consideration of the steep rotation gradients near the top and bottom surfaces, two different bias meshes, as shown in Figure 9, that are respectively composed of 32×12 elements and 40×16 elements are used. Besides, the angular distortions are also introduced for testing the element's tolerance to the mesh distortion. Good agreements are observed between the numerical results and the analytical reference solutions given in Figures 10 and 11, revealing that the new element can still capture the size dependence effectively in distorted meshes.

5.1.5 The cantilever thin beam

As illustrated in Figure 12, the micro thin beam is fully fixed at its left end and subjected to a uniformly distributed transverse load p at the right tip. The variation of the non-dimensional stiffness ratio K/K_0 versus the ratio h/l is evaluated with

$$K = \frac{pth}{v_{\text{tip}}}, \quad K_0 = \frac{3EI}{L^3}, \tag{88}$$

in which v_{tip} is the tip transverse deflection and I is the area moment of inertia. Two different ratios of beam length to height (L/h=20, 40) are considered.

As discussed in [45, 72], the non-dimensional stiffness will experience the so-called couple stress saturated status when the material length scale parameter is significantly larger than the beam thickness for which the continuity assumption of material is somewhat questionable. In this situation, the effects of the couple stress are dominated, locking up the bending behavior and leading to a nearly pure shear mode. In order to capture such extreme phenomenon, the refined mesh 100×10 is employed and the numerical results are provided in Figure 13. It's obvious that the present numerical results are in good agreement with the reference solutions which are obtained using the Lagrange multiplier FE formulation [42], accurately predicting the transition from classical case to saturated couple stress response. This test demonstrates once again that the new quadrilateral element can predict the size dependences well.

5.2. Tests for 3D consistent couple stress elasticity

5.2.1 The 3D patch test

The 3D patch test is examined to assess the convergence property of the new hexahedral element. Figure 14 illustrates the rectangular solid and two typical meshes composed of 2×2×2 elements including the regular one and distorted one. It can be verified easily that the element can always exactly reproduce the constant stress state. Therefore, only the results of the constant couple stress test are discussed here. To generate a deformation where the couple stresses are constant, the following equations are considered:

$$u = x^2 + y^2 + z^2 - 5xy, \quad v = x^2 + y^2 + z^2 - 5yz, \quad w = x^2 + y^2 + z^2 - 5xz, \tag{89}$$

$$\omega_x = -z + 3.5y, \quad \omega_y = -x + 3.5z, \quad \omega_z = -y + 3.5x. \tag{90}$$

The displacements and rotations calculated at the boundary nodes are imposed to the solid as the prescribed boundary conditions and the result of the central point A (0.15mm, 0.1mm, 0.1mm) are evaluated. The numerical results show that the element can strictly pass the test in the regular Mesh a but fails in the distorted Mesh b. This is mainly because that in the present development, the C^1

continuity requirement is satisfied in weak form and the quadratic part of displacement interpolation is incomplete in distorted mesh. Next, in order to further verify whether the element in distorted mesh can give acceptable results in this test, the computations are repeated by subdividing Mesh b. It is shown in Table 8 that the errors are effectively eliminated by the mesh refinement, from which we can conclude that the reliable results can be obtained by using the mesh of the desired quality.

5.2.2 Deformation of the hollow cylinder

As shown in Figure 15, the circular ring examined in Section 5.1.2 is extruded into a thick-walled hollow cylinder. All the degrees of freedom at the outer surface of the cylinder are restrained, and the boundary conditions at the internal surface are given by

$$u_\theta = 1.0\text{mm}, \quad u_r = w = 0. \tag{91}$$

The computations are operated by respectively dividing the cylinder into 10, 20 and 30 segments along the longitudinal direction whilst the cross section of the cylinder is modeled using 64×16 elements in accordance with the conclusions given in Section 5.1.2. Table 9 gives the convergence results of the circumferential displacement calculated at the point C $\left(\dfrac{a+b}{2}, 0, \dfrac{L}{2}\right)$ and the rotation calculated at the point A $\left(a, 0, \dfrac{L}{2}\right)$. Figure 16 shows the distributions of the displacement and rotation along the radial path AB. The analytical plain strain solutions [46] are also provided here for comparison. One can easily view that the new hexahedral element has good numerical accuracy and captures the size effect effectively.

5.2.3 Torsion of the slender cylindrical bar

As depicted in Figure 17, the slender solid cylinder is subjected to a torque Q at its right end, while the left end is constrained as

$$\omega_y = \omega_z = 0 \text{ at } x = 0, \ y = 0, \ z = 0, \tag{92}$$

$$u = v = w = \omega_x = 0 \text{ at } x = 0. \tag{93}$$

The outer surface of the cylinder is free. As stated in [4], for the consistent couple stress elasticity materials, the mean curvatures in this test vanish which means that no size effect exists in this

problem. Thus, the displacements and mechanical rotations are exactly in the form as in the classical theory. The model is meshed by ten equal segments along the longitudinal direction whilst three typical meshes shown in Figure 18 are employed to discretize the section plane. The convergence results of the displacement w and mechanical rotation ω_x at the point B for three different material length scale parameters are summarized in Table 10, in which the reference solutions are analytically calculated by

$$w = \varphi xy, \quad \omega_x = \varphi x, \quad \varphi = \frac{Q}{GI_p}, \tag{94}$$

where φ denotes the torsion angle per unit length and GI_p is the torsional rigidity of the cylinder. It is shown that the numerical results of the new hexahedral element converge very rapidly.

5.2.4 The simple shear problem of 3D block

The simple shear problem discussed in the previous is analyzed once again by considering a 3D block as shown in Figure 19. The bottom of the block is clamped while the top surface is forced to deform as

$$u = 1\,\mu m, \quad v = w = \omega_x = \omega_y = \omega_z = 0. \tag{95}$$

The computation is performed by using the bias mesh 40×16×10 which is the extrusion of the angularly distorted Mesh b given in Figure 9 along the z-direction. As demonstrated in Figure 20 where the distributions of displacement u and rotation ω_z along the path $(x = 0.5L, z = 0.5L)$ is provided, the proposed hexahedral element also has good numerical accuracy in distorted meshes.

5.2.5 The 3D cantilever thin beam

As shown in Figure 21, this test involves the deformation of the 3D cantilever thin beam subjected to a uniformly distributed transverse load at the right end. The beam is fully fixed at the left end with the constraints $u = v = w = \omega_x = \omega_y = \omega_z = 0$ while is free at its lateral surfaces. First, the stiffness of the 3D thin beam, which is calculated by substituting the tip transverse deflection at the symmetry plane $(z = t/2)$ into Equation (88), is investigated. Table 11 gives the convergence results of the case with t=10h for different material length scale parameters. One can see that the

material length scale parameter has some slight influences on the convergence rate. In general, the larger l is, the slower results converge. Besides, the stiffness of the 3D thin beams with different widths is analyzed. It is known that the solutions of 3D cases will gradually approach the plane strain solution as the beam width increases [72]. Thus, in order to reproduce the plane strain deformation state more correctly, the case $t/h=1$ is considered by imposing the following extra constrains to the beam's two lateral surfaces:

$$w = \omega_x = \omega_y = 0. \tag{96}$$

As could be seen from Figure 22, the new hexahedral element predicts the size-dependent behaviors very well and accurately captures the saturated couple stress state as well as the transition process. Next, to illustrate the difference between the plane strain deformation state and fully 3D deformation state more clearly, the beam with $t/h=10$ and $l/h=1.0$ is analyzed again by considering and not considering the lateral constrains shown in Equation (96). The contours of the displacement v, stress σ_{xx}, the couple stress μ_{xz} of the beam in these two deformation states are provided in Figure 23. One can see that the constraints acting on the beam lateral surfaces strongly affect the distribution of deformation.

5.2.6 Another 3D cantilever thin beam

As shown in Figure 24, this test also involves the deformation of a 3D cantilever thin beam, which is originally proposed in [72]. Different with the previous one, the beam is constrained at the left end with $u = v = w = 0$, and subjected to a concentrated force at the right end. First, the beam stiffness of the 3D thin beam with different ratios of the width to the height are given in Figure 25, in which the results have been normalized by the values obtained using the classical elasticity. Note that the stiffness here is calculated using the same treatment as that in [72], namely $K = P/v_{tip}$, for purpose of comparing the present results with those obtained by the Ritz spline method [72]. As can be seen from Figure 25, the present numerical results are in good agreement with the reference values. Next, the case with $t/h=4$ and $l/h=1$ is evaluated to show the difference between the two different deformation state with and without considering the lateral constraints given in Equation (96). Figure 26 illustrates the distributions of the displacement v and couple stress μ_{xz} on the top

surface of the beam. It is shown that the displacement results agree with those proposed in [72] well. But the couple stress results are smaller than those in [72], although they have the similar distribution.

5. Conclusions

The consistent couple stress theory [4] has been demonstrated as a promising theory that can effectively capture the size effects of small-scale structures but requires the reliable numerical approaches for practical applications. In this paper, the penalty unsymmetric finite element framework is established for the consistent couple stress elasticity materials and then, C^0 8-node quadrilateral element and 20-node hexahedral element are developed. In the present developments, the C^1 continuity requirement is enforced by using the penalty function method in conjunction with the usage of independently introduced rotation DOFs. Consequently, the test functions of the displacement and mechanical rotation can be separately formulated by using C^0 shape functions, from which the test functions of the strain and mean curvature are further derived. Besides, the trial functions of the stress and couple stress are constructed based on stress functions which are derived from the equilibrium equations of considered problems. Several benchmark tests involving different deformation modes are carried out by comparison with known in literature results, to validate the proposed elements' performances. It is found that both the new 2D quadrilateral element and 3D hexahedral element can predict the size-dependent mechanical behaviors of consistent couple stress elasticity materials very efficiently and exhibits the advantages of the unsymmetric FEM, such as the concise formulation, good numerical accuracy and high tolerance to mesh distortion.

Data Availability Statement

Data are available on request from the authors.

References

[1] R.A. Toupin, Elastic materials with couple-stresses, Archive for Rational Mechanics and Analysis 11(1) (1962) 385-414.

[2] R.D. Mindlin, H.F. Tiersten, Effects of couple-stresses in linear elasticity, Archive for Rational Mechanics and Analysis 11(1) (1962) 415-448.

[3] W.T. Koiter, Couple-stress in the theory of elasticity, Proc.k.ned.akad.wet 67 (1964).

[4] A.R. Hadjesfandiari, G.F. Dargush, Couple stress theory for solids, International Journal of Solids and Structures 48(18) (2011) 2496-2510.

[5] N.A. Fleck, J.W. Hutchinson, A phenomenological theory for strain gradient effects in plasticity, Journal of the Mechanics and Physics of Solids 41(12) (1993) 1825-1857.

[6] R.D. Mindlin, N.N. Eshel, On first strain-gradient theories in linear elasticity, International Journal of Solids and Structures 4(1) (1968) 109-124.

[7] N.A. Fleck, J.W. Hutchinson, Strain gradient plasticity, Advances in Applied Mechanics 33 (1997) 295-361.

[8] N.A. Fleck, G.M. Muller, M.F. Ashby, J.W. Hutchinson, Strain gradient plasticity: theory and experiment, Acta Metallurgica et Materialia 42(2) (1994) 475-487.

[9] M. Shaat, E. Ghavanloo, S.A. Fazelzadeh, Review on nonlocal continuum mechanics: physics, material applicability, and mathematics, Mechanics of Materials 150 (2020) 103587.

[10] A.C. Eringen, D.G.B. Edelen, On nonlocal elasticity, International Journal of Engineering Science 10(3) (1972) 233-248.

[11] A.C. Eringen, Linear theory of nonlocal elasticity and dispersion of plane waves, International Journal of Engineering Science 10(5) (1972) 425-435.

[12] E. Cosserat, Theorie des corps deformables, Herman et Fils Paris (1909).

[13] F. Yang, A.C.M. Chong, D.C.C. Lam, P. Tong, Couple stress based strain gradient theory for elasticity, International Journal of Solids and Structures 39(10) (2002) 2731-2743.

[14] S.L. Kong, A review on the size-dependent models of micro-beam and micro-plate based on the modified couple stress theory, Archives of Computational Methods in Engineering 29(1) (2022) 1-31.

[15] G. Rizzi, G. Hütter, A. Madeo, P. Neff, Analytical solutions of the simple shear problem for micromorphic models and other generalized continua, Archive of Applied Mechanics 91(5)

(2021) 2237-2254.

[16] I. Münch, P. Neff, A. Madeo, I.D. Ghiba, The modified indeterminate couple stress model: Why Yang et al.'s arguments motivating a symmetric couple stress tensor contain a gap and why the couple stress tensor may be chosen symmetric nevertheless, ZAMM-Journal of Applied Mathematics and Mechanics/Zeitschrift für Angewandte Mathematik und Mechanik 97(12) (2017) 1524-1554.

[17] P. Neff, I. Münch, I.D. Ghiba, A. Madeo, On some fundamental misunderstandings in the indeterminate couple stress model. A comment on recent papers of AR Hadjesfandiari and GF Dargush, International Journal of Solids and Structures 81 (2016) 233-243.

[18] A.R. Hadjesfandiari, Size-dependent piezoelectricity, International Journal of Solids and Structures 50(18) (2013) 2781-2791.

[19] A.R. Hadjesfandiari, Size-dependent thermoelasticity, Latin American Journal of Solids and Structures 11(9) (2014) 1679-1708.

[20] S.E. Alavi, M. Sadighi, M.D. Pazhooh, J.F. Ganghoffer, Development of size-dependent consistent couple stress theory of Timoshenko beams, Applied Mathematical Modelling 79 (2020) 685-712.

[21] B.N. Patel, D. Pandit, S.M. Srinivasan, A simplified moment-curvature based approach for large deflection analysis of micro-beams using the consistent couple stress theory, European Journal of Mechanics a-Solids 66 (2017) 45-54.

[22] A.Q. Li, S.J. Zhou, S.S. Zhou, B.L. Wang, Size-dependent analysis of a three-layer microbeam including electromechanical coupling, Composite Structures 116 (2014) 120-127.

[23] S.F. Dehkordi, Y.T. Beni, Electro-mechanical free vibration of single-walled piezoelectric/flexoelectric nano cones using consistent couple stress theory, International Journal of Mechanical Sciences 128-129 (2017) 125-139.

[24] C.G. Subramaniam, P.K. Mondal, Effect of couple stresses on the rheology and dynamics of linear Maxwell viscoelastic fluids, Physics of Fluids 32(1) (2020) 013108.

[25] C.P. Wu, H.X. Hu, A unified size-dependent plate theory for static bending and free vibration analyses of micro- and nano-scale plates based on the consistent couple stress theory, Mechanics of Materials 162 (2021) 104085.

[26] Y.L. Qu, P. Li, F. Jin, A general dynamic model based on Mindlin's high-frequency theory and the microstructure effect, Acta Mechanica 231(9) (2020) 3847-3869.

[27] K.Y. Sze, W.C. Yuan, Y.X. Zhou, Four-node tetrahedral elements for gradient-elasticity analysis, International Journal for Numerical Methods in Engineering 121(16) (2020) 3660-3679.

[28] S. Cen, C.J. Wu, Z. Li, Y. Shang, C.F. Li, Some advances in high-performance finite element methods, Engineering Computations 36(8) (2019) 2811-2834.

[29] M.H. Kahrobaiyan, M. Asghari, M.T. Ahmadian, A Timoshenko beam element based on the modified couple stress theory, International Journal of Mechanical Sciences 79 (2014) 75-83.

[30] A.M. Dehrouyeh-Semnani, A. Bahrami, On size-dependent Timoshenko beam element based on modified couple stress theory, International Journal of Engineering Science 107 (2016) 134-148.

[31] J.N. Reddy, J. Romanoff, J. Antonio Loya, Nonlinear finite element analysis of functionally graded circular plates with modified couple stress theory, European Journal of Mechanics a-Solids 56 (2016) 92-104.

[32] B. Zhang, Y.M. He, D.B. Liu, Z.P. Gan, L. Shen, A non-classical Mindlin plate finite element based on a modified couple stress theory, European Journal of Mechanics a-Solids 42 (2013) 63-80.

[33] Y. Shang, Y.H. Mao, S. Cen, C.F. Li, Generalized conforming Trefftz element for size-dependent analysis of thin microplates based on the modified couple stress theory, Engineering Analysis with Boundary Elements 125 (2021) 46-58.

[34] I. Soleimani, Y.T. Beni, F. Mehralian, A new size-dependent cylindrical shell element based on modified couple stress theory, Advances in Applied Mathematics and Mechanics 10(4) (2018) 819-844.

[35] Y. Shang, H.P. Wu, S. Cen, C.F. Li, An efficient 4-node facet shell element for the modified couple stress elasticity, International Journal for Numerical Methods in Engineering 123(4) (2022) 992-1012.

[36] C.S. Wang, X.K. Zhang, P. Hu, Assumed stress quasi-conforming triangular element for couple stress theory, Acta Mechanica Solida Sinica 30(4) (2017) 335-344.

[37] X. Ma, W.J. Chen, Refined 18-DOF triangular hybrid stress element for couple stress theory, Finite Elements in Analysis and Design 75 (2013) 8-18.

[38] J.H. Choi, B.C. Lee, A 3-node C^0 triangular element for the modified couple stress theory based on the smoothed finite element method, International Journal for Numerical Methods in Engineering 114(12) (2018) 1245-1261.

[39] Y.R. Kwon, B.C. Lee, A mixed element based on Lagrange multiplier method for modified couple stress theory, Computational Mechanics 59(1) (2017) 117-128.

[40] Y.R. Kwon, B.C. Lee, Three dimensional elements with Lagrange multipliers for the modified couple stress theory, Computational Mechanics 62(1) (2018) 97-110.

[41] J.H. Choi, B.C. Lee, G.D. Sim, A 10-node tetrahedral element with condensed Lagrange

multipliers for the modified couple stress theory, Computers & Structures 246 (2021) 106476.

[42] B.T. Darrall, G.F. Dargush, A.R. Hadjesfandiari, Finite element Lagrange multiplier formulation for size-dependent skew-symmetric couple-stress planar elasticity, Acta Mechanica 225(1) (2014) 195-212.

[43] G.Q. Deng, G.F. Dargush, Mixed Lagrangian formulation for size-dependent couple stress elastodynamic and natural frequency analyses, International Journal for Numerical Methods in Engineering 109(6) (2017) 809-836.

[44] G.Q. Deng, G.F. Dargush, Mixed Lagrangian formulation for size-dependent couple stress elastodynamic response, Acta Mechanica 227(12) (2016) 3451-3473.

[45] A. Pedgaonkar, B.T. Darrall, G.F. Dargush, Mixed displacement and couple stress finite element method for anisotropic centrosymmetric materials, European Journal of Mechanics a-Solids 85 (2021) 104074.

[46] S. Chakravarty, A.R. Hadjesfandiari, G.F. Dargush, A penalty-based finite element framework for couple stress elasticity, Finite Elements in Analysis and Design 130 (2017) 65-79.

[47] R. Poya, A.J. Gil, R. Ortigosa, R. Palma, On a family of numerical models for couple stress based flexoelectricity for continua and beams, Journal of the Mechanics and Physics of Solids 125 (2019) 613-652.

[48] B.T. Darrall, A.R. Hadjesfandiari, G.F. Dargush, Size-dependent piezoelectricity: A 2D finite element formulation for electric field-mean curvature coupling in dielectrics, European Journal Of Mechanics a-Solids 49 (2015) 308-320.

[49] A.R. Hadjesfandiari, G.F. Dargush, Boundary element formulation for plane problems in couple stress elasticity, International Journal for Numerical Methods in Engineering 89(5) (2012) 618-636.

[50] A.R. Hadjesfandiari, A. Hajesfandiari, G.F. Dargush, Size-dependent contact mechanics via boundary element analysis. Engineering Analysis with Boundary Elements 136 (2022) 213-231.

[51] J. Lei, P.S. Ding, C.Z. Zhang, Boundary element analysis of static plane problems in size-dependent consistent couple stress elasticity, Engineering Analysis with Boundary Elements 132 (2021) 399-415.

[52] S. Rajendran, K.M. Liew, A novel unsymmetric 8-node plane element immune to mesh distortion under a quadratic displacement field, International Journal for Numerical Methods in Engineering 58(11) (2003) 1713-1748.

[53] S. Cen, P.L. Zhou, C.F. Li, C.J. Wu, An unsymmetric 4-node, 8-DOF plane membrane element perfectly breaking through MacNeal's theorem, International Journal for Numerical Methods in Engineering 103(7) (2015) 469-500.

[54] Q. Xie, K.Y. Sze, Y.X. Zhou, Modified and Trefftz unsymmetric finite element models, International Journal of Mechanics and Materials in Design 12(1) (2016) 53-70.

[55] Z. Li, S. Cen, C.J. Wu, Y. Shang, C.F. Li, High-performance geometric nonlinear analysis with the unsymmetric 4-node, 8-DOF plane element US-ATFQ4, International Journal for Numerical Methods in Engineering 114(9) (2018) 931-954.

[56] J.B. Huang, S. Cen, Z. Li, C.F. Li, An unsymmetric 8-node hexahedral solid-shell element with high distortion tolerance: linear formulations, International Journal for Numerical Methods in Engineering 116(12-13) (2018) 759-783.

[57] Z. Li, S. Cen, J.B. Huang, C.F. Li, Hyperelastic finite deformation analysis with the unsymmetric finite element method containing homogeneous solutions of linear elasticity, International Journal for Numerical Methods in Engineering 121(16) (2020) 3702-3721.

[58] Y. Shang, Y.D. Liu, S.X. Liu, Trefftz-unsymmetric finite element for bending analysis of orthotropic plates, Engineering with Computers (2021).

[59] Y. Shang, Z.H. Qian, S. Cen, C.F. Li, A simple unsymmetric 4-node 12-DOF membrane element for the modified couple stress theory, International Journal for Numerical Methods in Engineering 119(9) (2019) 807-825.

[60] Y. Shang, C.F. Li, K.Y. Jia, 8-node hexahedral unsymmetric element with rotation DOFs for modified couple stress elasticity, International Journal for Numerical Methods in Engineering 121(12) (2020) 2683-2700.

[61] Y. Shang, H.P. Wu, Couple stress-based unsymmetric 8-node planar membrane elements with good tolerances to mesh distortion. Engineering Computations, 39(2) (2022) 1097-1117.

[62] D.J. Allman, A compatible triangular element including vertex rotations for plane elasticity analysis, Computers & Structures 19(1-2) (1984) 1-8.

[63] D.J. Allman, A quadrilateral finite element including vertex rotations for plane elasticity analysis, International Journal for Numerical Methods in Engineering 26(3) (1988) 717-730.

[64] Y. Shang, W.G. Ouyang, 4-node unsymmetric quadrilateral membrane element with drilling DOFs insensitive to severe mesh-distortion, International Journal for Numerical Methods in Engineering 113(10) (2018) 1589-1606.

[65] S. Cen, X.R. Fu, M.J. Zhou, 8-and 12-node plane hybrid stress-function elements immune to severely distorted mesh containing elements with concave shapes, Computer Methods in Applied Mechanics and Engineering 200(29-32) (2011) 2321-2336.

[66] N. Garg, C.S. Han, A penalty finite element approach for couple stress elasticity, Computational Mechanics 52(3) (2013) 709-720.

[67] Y. Shang, S. Cen, Z.H. Qian, C. Li, High-performance unsymmetric 3-node triangular

membrane element with drilling DOFs can correctly undertake in-plane moments, Engineering Computations 35(7) (2018) 2543-2556.

[68] V.M. Calo, N.O. Collier, A.H. Niemi, Analysis of the discontinuous Petrov-Galerkin method with optimal test functions for the Reissner-Mindlin plate bending model, Computers & Mathematics with Applications 66(12) (2014) 2570-2586.

[69] A.H. Niemi, J.A. Bramwell, L.F. Demkowicz, Discontinuous Petrov-Galerkin method with optimal test functions for thin-body problems in solid mechanics, Computer Methods in Applied Mechanics And Engineering 200(9-12) (2011) 1291-1300.

[70] A.K. Soh, W. J. Chen, Finite element formulations of strain gradient theory for microstructures and the C0-1 patch test, International Journal for Numerical Methods in Engineering 61(3) (2004) 433-454.

[71] S.K. Park, X.L. Gao, Variational formulation of a modified couple stress theory and its application to a simple shear problem, Zeitschrift für Angewandte Mathematik und Physik 59(5) (2008) 904-917.

[72] G.F. Dargush, G. Apostolakis, A.R. Hadjesfandiari, Two- and three-dimensional size-dependent couple stress response using a displacement-based variational method, European Journal of Mechanics a-Solids 88 (2021) 104268.

Table 1. Fifteen groups of the stress functions in the matrix $\mathbf{H}^n$ in Equation (49)

	i	1	2	3	4	5	6	7	8	9	10
	$\sigma^i_{(xx)}$	0	0	2	0	0	$2x$	$6y$	0	$6xy$	$-12y^2$
$\mathbf{H}^n_i$	$\sigma^i_{(yy)}$	2	0	0	$6x$	$2y$	0	0	$6xy$	0	$12x^2$
	$\sigma^i_{(xy)}$	0	-1	0	0	$-2x$	$-2y$	0	$-3x^2$	$-3y^2$	0

	i	11	12	13	14	15
	$\sigma^i_{(xx)}$	$12(x^2-y^2)$	$2x(x^2-6y^2)$	$10x^3$	$6x^2y$	$10y(3x^2-2y^2)$
$\mathbf{H}^n_i$	$\sigma^i_{(yy)}$	$-12(x^2-y^2)$	$6xy^2$	$-10x(2x^2-3y^2)$	$-2y(6x^2-y^2)$	$10y^3$
	$\sigma^i_{(xy)}$	$-24xy$	$-2y(3x^2-2y^2)$	$-30x^2y$	$2x(2x^2-3y^2)$	$-30xy^2$

Table 2. Forty-eight groups of the stress functions in the matrix $\mathbf{H}^n$ in Equation (77)

	i	1	2	3	4	5	6	7	8	9	10
$\mathbf{H}_i^n$	$\sigma^i_{(xx)}$	1	0	0	0	0	0	0	0	0	0
	$\sigma^i_{(yy)}$	0	1	0	0	0	0	x	0	$-y$	0
	$\sigma^i_{(zz)}$	0	0	1	0	0	0	0	x	0	0
	$\sigma^i_{(xy)}$	0	0	0	1	0	0	0	0	x	0
	$\sigma^i_{(yz)}$	0	0	0	0	1	0	0	0	0	x
	$\sigma^i_{(xz)}$	0	0	0	0	0	1	0	0	0	0

	i	11	12	13	14	15	16	17	18	19	20
$\mathbf{H}_i^n$	$\sigma^i_{(xx)}$	0	y	0	$-x$	0	0	z	0	0	0
	$\sigma^i_{(yy)}$	0	0	0	0	0	0	0	z	0	$-y$
	$\sigma^i_{(zz)}$	$-z$	0	y	0	$-z$	0	0	0	0	0
	$\sigma^i_{(xy)}$	0	0	0	y	0	0	0	0	z	0
	$\sigma^i_{(yz)}$	0	0	0	0	y	0	0	0	0	z
	$\sigma^i_{(xz)}$	x	0	0	0	0	y	0	0	0	0

	i	21	22	23	24	25	26	27	28	29	30
$\mathbf{H}_i^n$	$\sigma^i_{(xx)}$	$-x$	0	0	0	0	0	y^2	0	$-2xy$	0
	$\sigma^i_{(yy)}$	0	x^2	0	$-2xy$	0	0	0	0	0	0
	$\sigma^i_{(zz)}$	0	0	x^2	0	0	$-2xz$	0	y^2	0	$-2yz$
	$\sigma^i_{(xy)}$	0	0	0	x^2	0	0	0	0	y^2	0
	$\sigma^i_{(yz)}$	0	0	0	0	x^2	0	0	0	0	y^2

$\sigma^i_{(xz)}$	z	0	0	0	0	x^2	0	0	0	0

	i	31	32	33	34	35	36	37	38	39	40
	$\sigma^i_{(xx)}$	0	z^2	0	0	0	$-2xz$	0	$-x^2/2$	0	0
	$\sigma^i_{(yy)}$	0	0	z^2	0	$-2yz$	0	0	$-y^2/2$	0	0
	$\sigma^i_{(zz)}$	0	0	0	0	0	0	xy	0	$-xz$	$-yz$
$\mathbf{H}^n_i$	$\sigma^i_{(xy)}$	0	0	0	z^2	0	0	0	xy	0	0
	$\sigma^i_{(yz)}$	0	0	0	0	z^2	0	0	0	xy	0
	$\sigma^i_{(xz)}$	y^2	0	0	0	0	z^2	0	0	0	xy

	i	41	42	43	44	45	46	47	48
	$\sigma^i_{(xx)}$	yz	$-xz$	0	$-xy$	0	0	0	$-x^2/2$
	$\sigma^i_{(yy)}$	0	0	$-y^2/2$	0	xz	$-yz$	$-xy$	0
	$\sigma^i_{(zz)}$	0	0	$-z^2/2$	0	0	0	0	$-z^2/2$
$\mathbf{H}^n_i$	$\sigma^i_{(xy)}$	0	yz	0	0	0	xz	0	0
	$\sigma^i_{(yz)}$	0	0	yz	0	0	0	xz	0
	$\sigma^i_{(xz)}$	0	0	0	yz	0	0	0	xz

Table 3. Twenty-seven groups of the couple stress functions in the matrix $\mathbf{H}^c$ in Equation (77)

	i	1	2	3	4	5	6	7	8	9	10
$\mathbf{H}_i^c$	μ_{xy}^i	1	0	0	x	0	0	y	0	0	z
	μ_{yz}^i	0	1	0	0	x	0	0	y	0	0
	μ_{xz}^i	0	0	1	0	0	x	0	0	y	0

	i	11	12	13	14	15	16	17	18	19	20
$\mathbf{H}_i^c$	μ_{xy}^i	0	0	x^2	0	$-2yz$	y^2	0	0	z^2	0
	μ_{yz}^i	z	0	$2xz$	x^2	0	$2xz$	y^2	0	0	z^2
	μ_{xz}^i	0	z	0	0	x^2	0	$-2xy$	y^2	0	$-2xy$

	i	21	22	23	24	25	26	27
$\mathbf{H}_i^c$	μ_{xy}^i	$-2yz$	xy	$-yz$	0	0	xz	0
	μ_{yz}^i	0	0	xy	yz	xz	0	0
	μ_{xz}^i	z^2	0	0	0	yz	xy	xz

Table 4. The coefficients used for the 2D patch tests

Description	a_1	a_2	a_3	a_4	a_5	b_1	b_2	b_3	b_4	b_5
Constant stress	0	1	1	0	0	0	1	1	0	0
Constant couple stress	0	0	0	1	1	0	0	0	1	1

Table 5. The convergence results calculated at the characteristic points of the circular ring

	$M{\times}N$	16×4	32×8	64×16	128×32	Reference [46]
	l/a=0.25	0.3195	0.3030	0.2988	0.2977	0.297
$u_{\theta C}$ (mm)	l/a=0.5	0.3036	0.2750	0.2687	0.2668	0.266
	l/a=1	0.3245	0.2697	0.2584	0.2547	0.254
	l/a=0.25	-0.4672	-0.4626	-0.4620	-0.4616	-0.462
ω_{zA}	l/a=0.5	-0.5264	-0.5227	-0.5223	-0.5219	-0.522
	l/a=1	-0.5303	-0.5429	-0.5471	-0.5480	-0.548
	l/a=0.25	-2.9186	-2.9128	-2.9189	-2.9222	-2.923
$\sigma_{(r\theta)A}$ (MPa)	l/a=0.5	-2.9692	-3.0058	-3.0181	-3.0314	-3.044
	l/a=1	-2.7066	-2.9193	-2.9662	-3.0295	-3.097
	l/a=0.25	0.4107	0.4379	0.4463	0.4500	0.453
μ_{rzB} (N/mm)	l/a=0.5	1.2291	1.2614	1.2698	1.2744	1.278
	l/a=1	4.1936	4.3469	4.3873	4.4035	4.414

Table 6. The convergence results of the nominal stress concentration factors

l/a	Mesh a	Mesh b	Mesh c	Reference [49]
0.0001	3.19263	3.19406	3.19462	3.1935
0.01	3.18656	3.18757	3.19160	3.1911
0.1	2.76187	2.77017	2.77690	2.7843
0.25	1.96916	1.98575	1.99417	2.0058
0.5	1.46169	1.47944	1.48766	1.4998
1	1.25037	1.26698	1.27473	1.2866

Table 7. The convergence results of the horizontal displacements at the points B and C

	l/a	Mesh a	Mesh b	Mesh c	Reference [49]
u_C (mm)	0.0001	0.14685	0.14643	0.14640	0.1464
	0.01	0.14763	0.14726	0.14723	0.1472
	0.1	0.21082	0.21130	0.21130	0.2113
	0.25	0.35529	0.35574	0.35573	0.3557
	0.5	0.46338	0.46211	0.46188	0.4617
	1	0.51366	0.51095	0.51051	0.5102
u_B (mm)	0.0001	1.46407	1.46350	1.46339	1.4634
	0.01	1.46178	1.46115	1.46101	1.4610
	0.1	1.29072	1.28824	1.28759	1.2868
	0.25	0.94304	0.94038	0.93970	0.9387
	0.5	0.70840	0.70633	0.70582	0.7051
	1	0.60692	0.60493	0.60446	0.6038

Table 8. The results of the 3D constant couple stress test

Mesh	8 elements	64 elements	512 elements	Exact solution
u_A (mm)	-0.03243	-0.03244	-0.03249	-0.0325
v_A (mm)	-0.00814	-0.00741	-0.00750	-0.0075
w_A (mm)	-0.03247	-0.03249	-0.03250	-0.0325
μ_{xyA} (N/mm)	-0.713	-0.718	-0.720	-0.72
μ_{yzA} (N/mm)	-0.713	-0.716	-0.720	-0.72
μ_{xzA} (N/mm)	0.750	0.723	0.720	0.72

Table 9. The convergence results calculated at the characteristic points of the hollow cylinder

	Longitudinal mesh	10	20	30	Reference [46]
	l/a=0.25	0.2985	0.2984	0.2984	0.297
$u_{\theta C}$ (mm)	l/a=0.5	0.2675	0.2674	0.2674	0.266
	l/a=1	0.2544	0.2543	0.2543	0.254
	l/a=0.25	-0.4432	-0.4428	-0.4429	-0.462
ω_{zA}	l/a=0.5	-0.5086	-0.5083	-0.5083	-0.522
	l/a=1	-0.5421	-0.5421	-0.5421	-0.548

Table 10. The convergence results of displacement and rotation the slender cylindrical bar

	l/R	12×10	48×10	192×10	Reference
w_B (μm)	0.1	122.209	122.018	122.013	
	1	122.208	122.029	122.014	122.02
	10	122.216	122.032	122.018	
ω_{xB}	0.1	12.2196	12.1995	12.2073	
	1	12.2210	12.2035	12.2021	12.202
	10	12.2214	12.2032	12.2022	

Table 11. The convergence results of stiffness of the 3D cantilever thin beam

	h/l	25×5×10	50×10×20	100×10×40	100×20×40
K/K_0	0.1	5.641	5.034	4.807	4.805
	1	3.915	3.744	3.697	3.696
	2	2.873	2.783	2.764	2.764
	5	1.661	1.638	1.633	1.633
	10	1.211	1.207	1.206	1.206
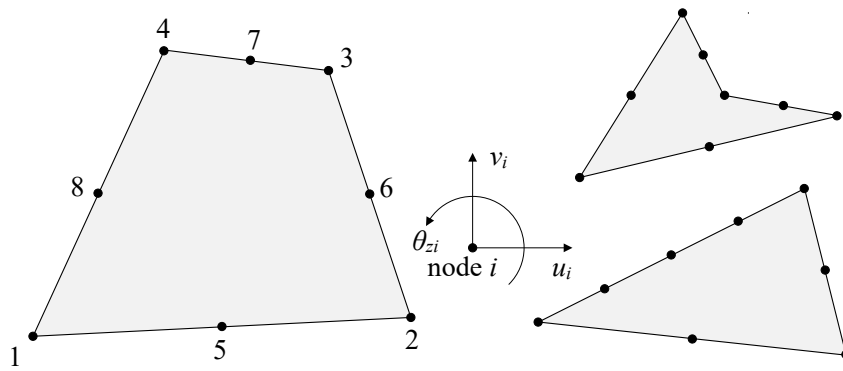
Figure 1. The new 8-node quadrilateral element based on the CCST
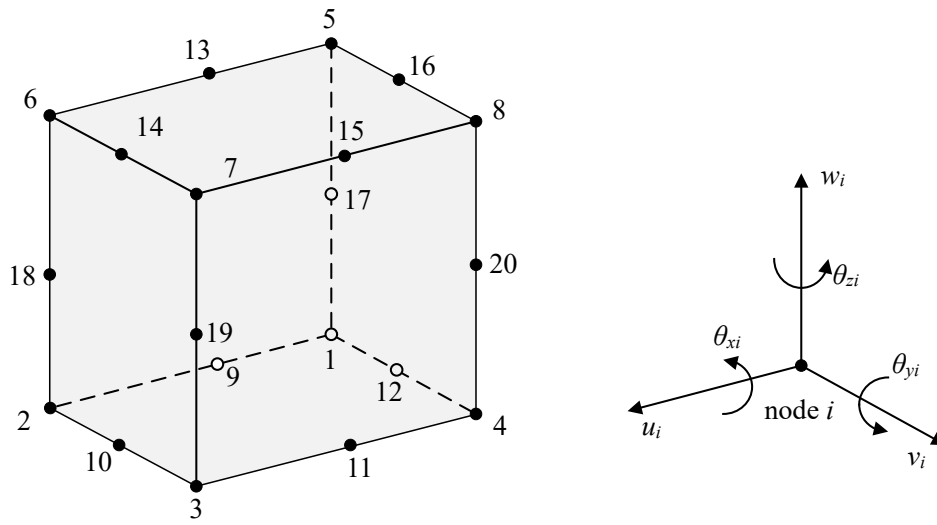
Figure 2. The new 20-node hexahedral element based on the CCST

Mesh a   Mesh b   Mesh c
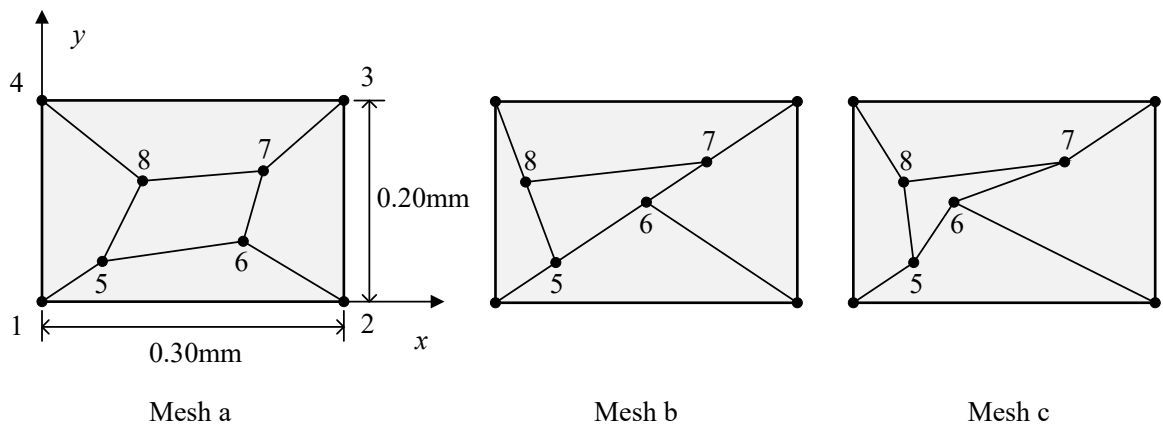
$E= 1.0\text{GPa}, v=0.25, l=17.6\mu\text{m}$

Figure 3. The typical meshes used for the 2D patch test
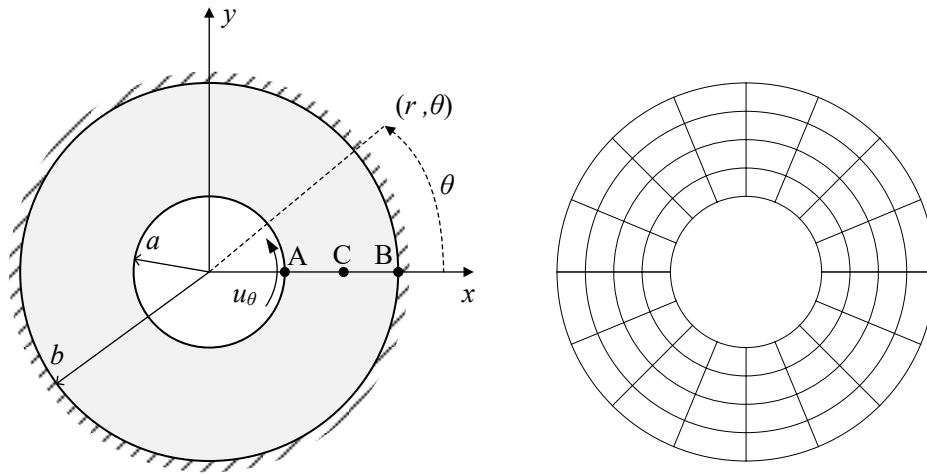
E=2.5MPa, v=0.25, a=1.0mm, b=2.0mm, Point C $\left(\dfrac{a+b}{2}, 0\right)$

Figure 4. The model of the circular ring and the typical mesh 16×4
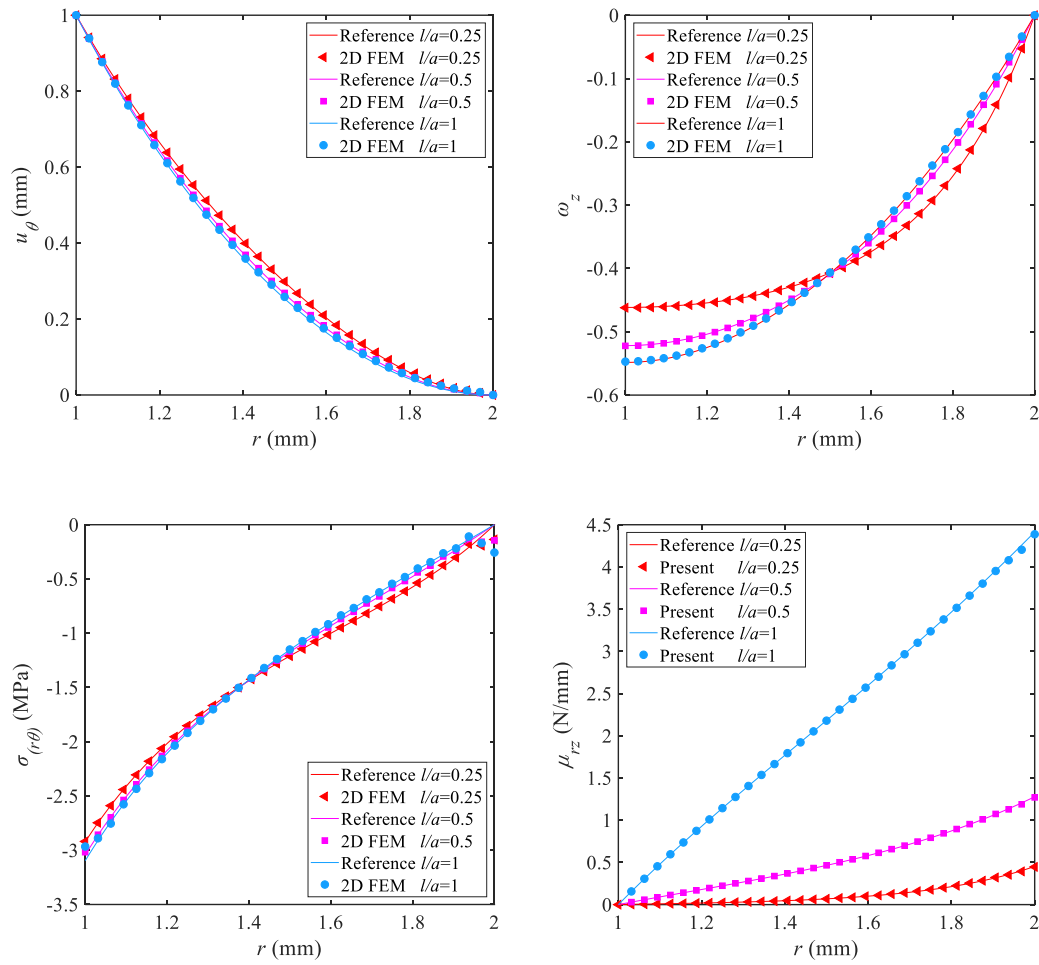
Figure 5. The distributions of the displacement, rotation, shear stress and couple stress along the radius obtained using the mesh 64×16
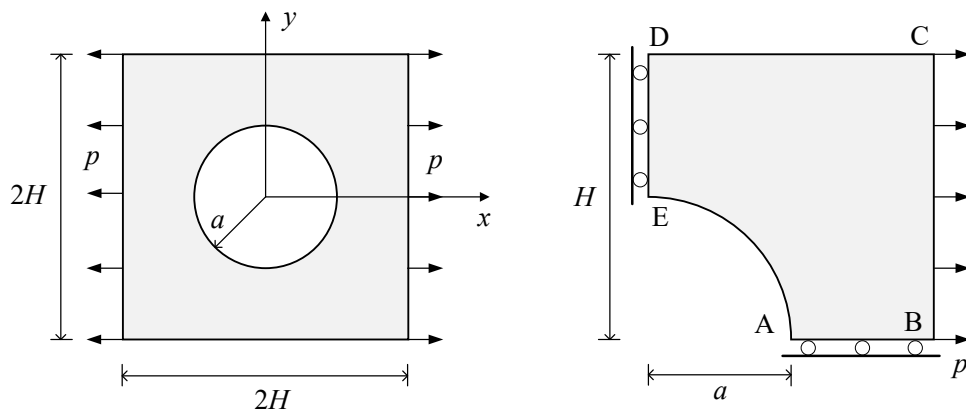
E=2.5MPa, v=0.25, H=2.0mm, a=1.0mm, p=0.5N/mm

Figure 6. The square plate with a hole
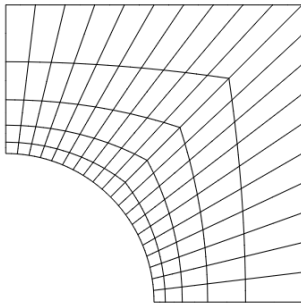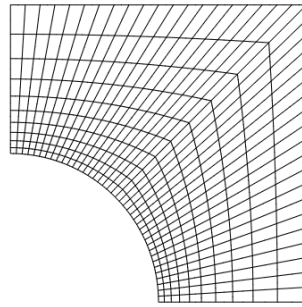
Mesh a: 100 elements   Mesh b: 400 elements   Mesh c: 900 elements
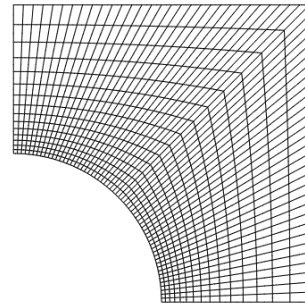
Figure 7. The typical meshes used for the square plate with a hole
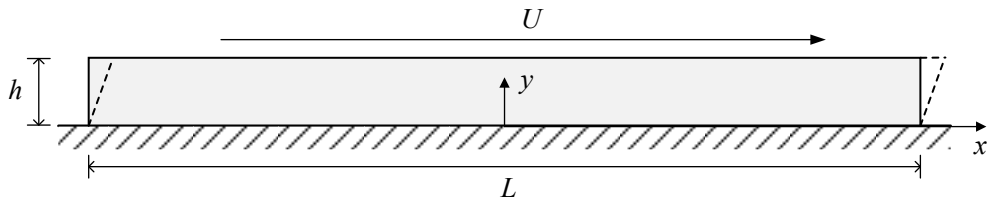
E=1.44GPa, v=0.38, h=100.0μm, L=10h, U=1.0μm

Figure 8. The 2D simple shear problem
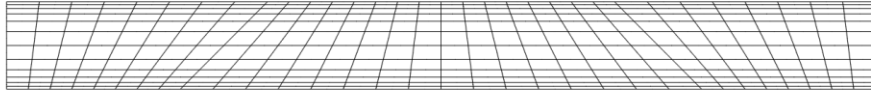
Mesh a: 32×12 elements
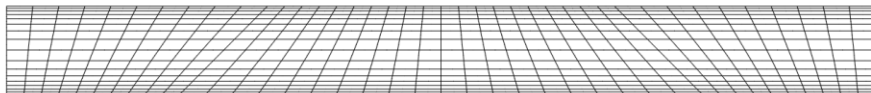
Mesh b: 40×16 elements

Figure 9. The bias meshes used for the 2D simple shear problem
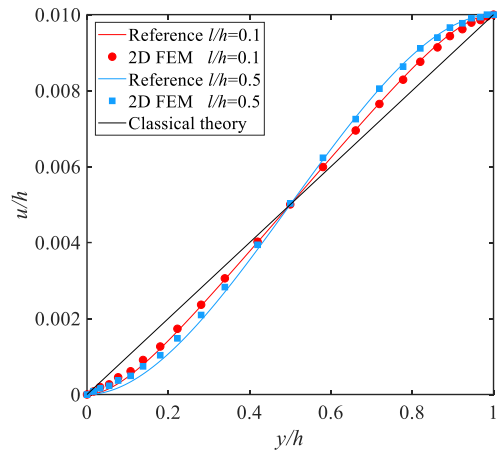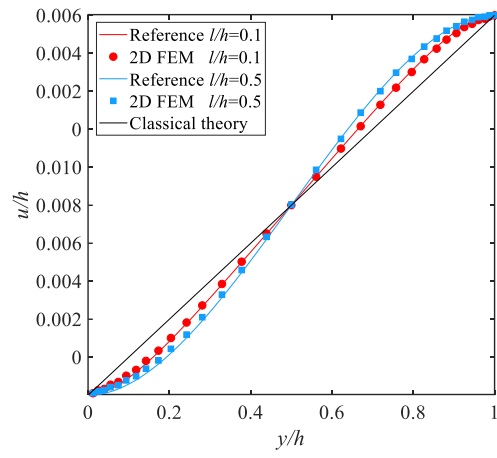
Mesh a   Mesh b

Figure 10. The distribution of displacement along *x*=0 of the 2D simple shear problem
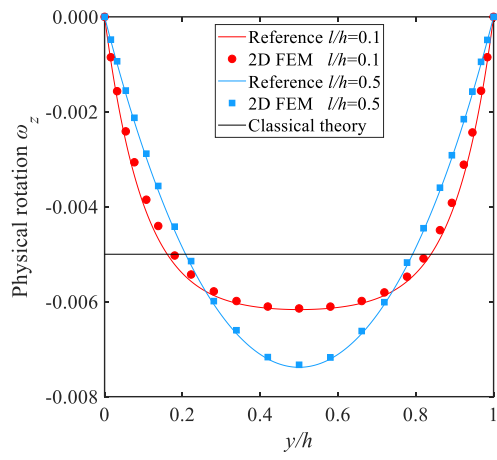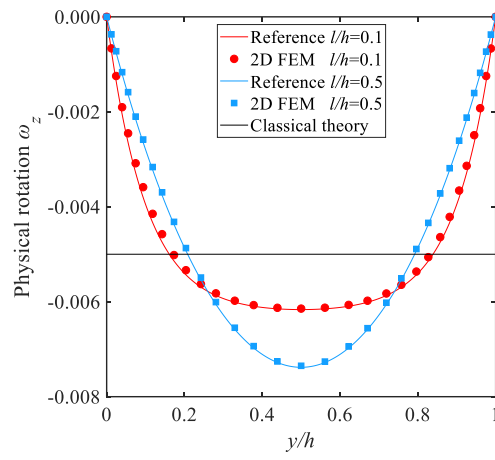
Mesh a   Mesh b

Figure 11. The distribution of rotation along x=0 of the 2D simple shear problem
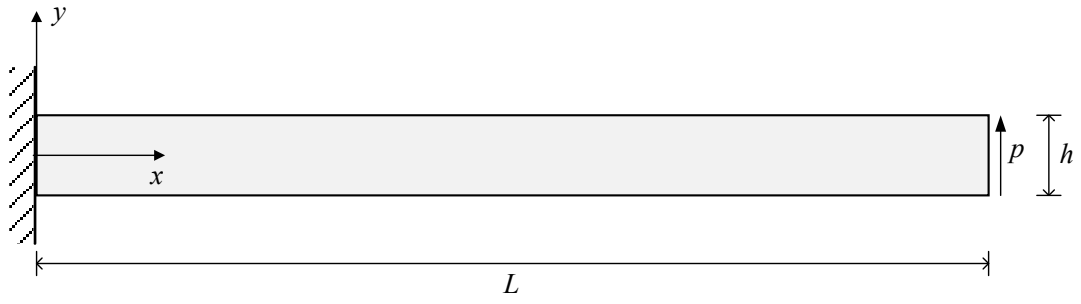
E=2.0MPa, v=0.0, width t=1mm, p=1.0N/mm^2

Figure 12. The 2D cantilever thin beam
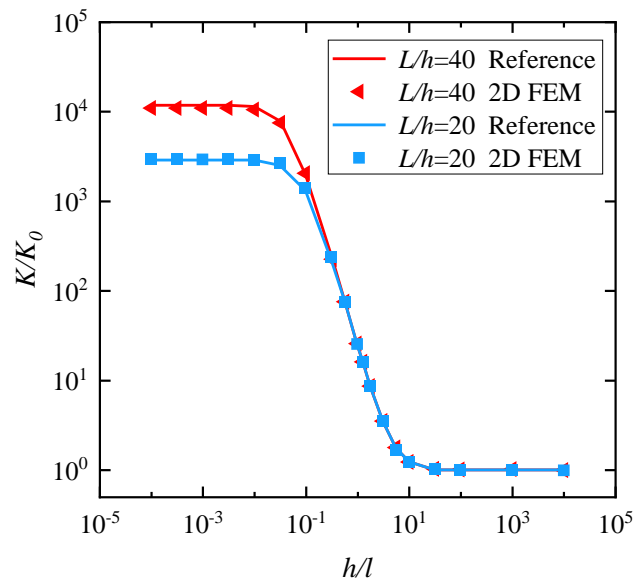
Figure 13. The stiffness of the 2Dcantilever thin beam

Mesh a   Mesh b
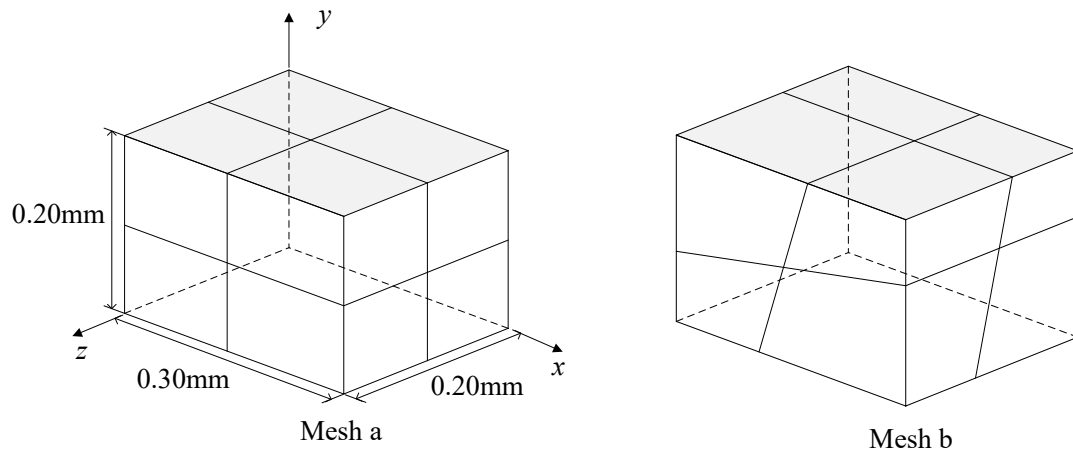
E= 1.0GPa, v=0.25, l=10.0μm

Figure 14. The typical meshes for the 3D patch test
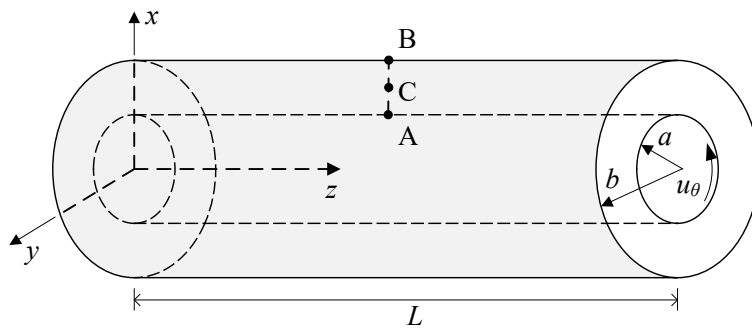
E=2.5MPa, *v*=0.25, *a*=1.0mm, *b*=2.0mm, *L*=10.0mm

Figure 15. The model of the hollow cylinder
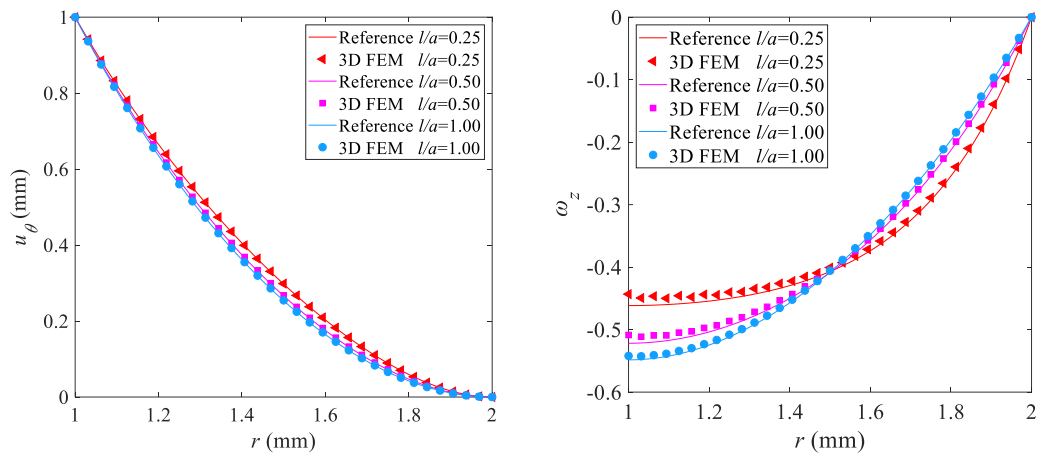
Figure 16. The distributions of the displacement and rotation along the radius of
the hollow cylinder obtained using the mesh 64×16×10

B (*L*/2, *R*, 0)

2*R*

x

z

L

Q
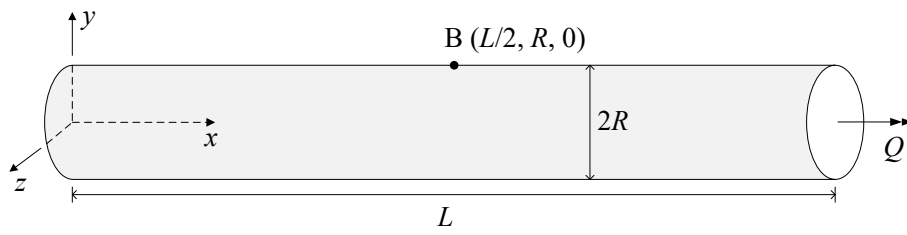
E=1.44GPa, *v*=0.38, *R*=10μm, *L*=20R, *Q*=1N·μm

Figure 17. Torsion of the slender cylindrical bar
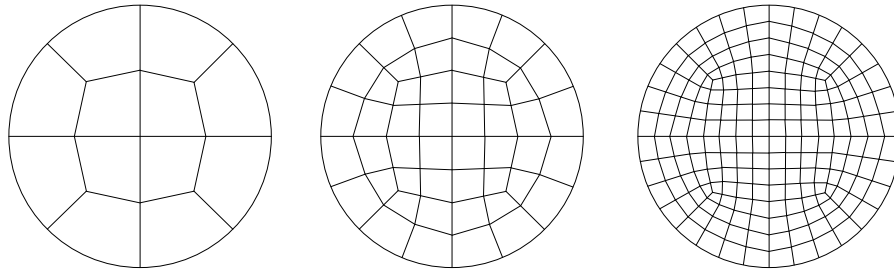
| (a) 12×10 elements | (b) 48×10 elements | (c) 192×10 elements |

Figure 18. The typical meshes for the slender cylindrical bar
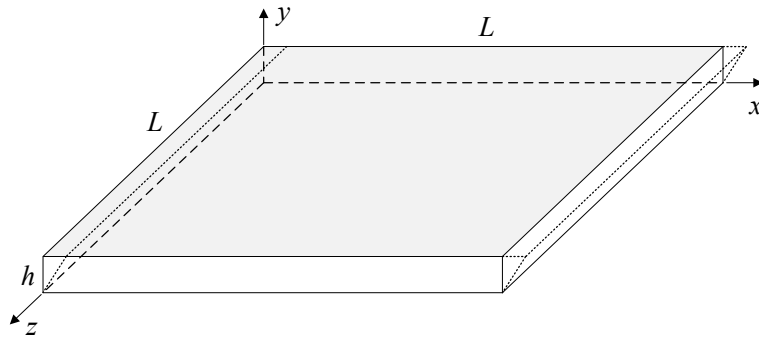
E=1.44GPa, *v*=0.38, *h*=100.0μm, *L*=10*h*, *U*=1.0μm

Figure 19. The simple shear problem of 3D block
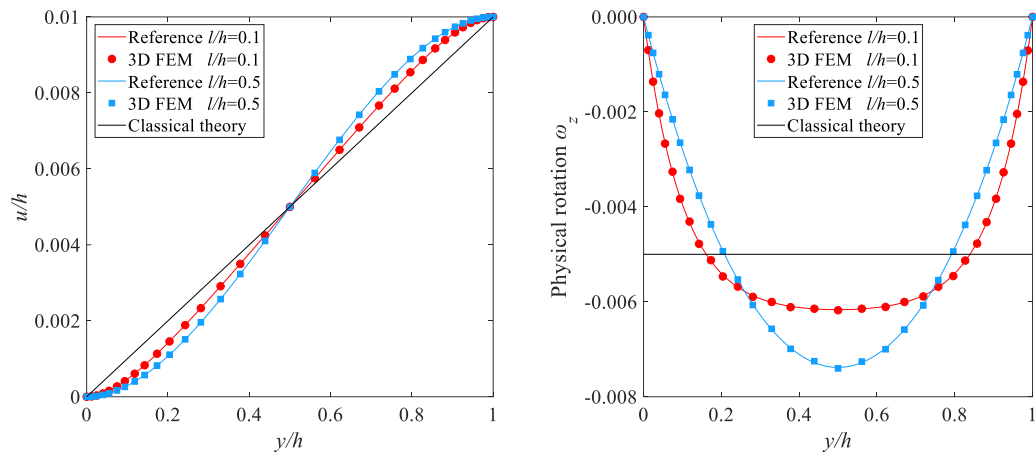
Figure 20. The distributions of the displacement and rotation along the path

(x=0.5L, z=0.5L) of the 3D block
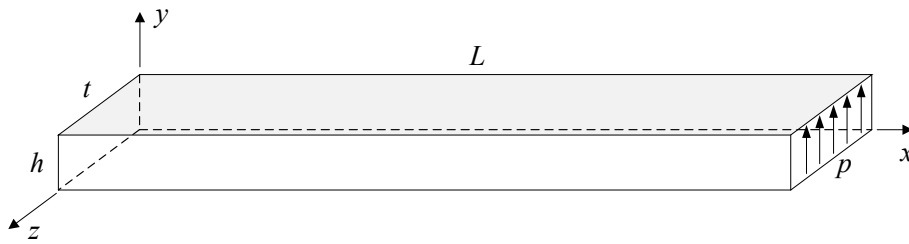
E=2.0MPa, v=0.0, p=1.0N/mm^2, h=1mm, L/h=20

Figure 21. The full fixed 3D cantilever thin beam
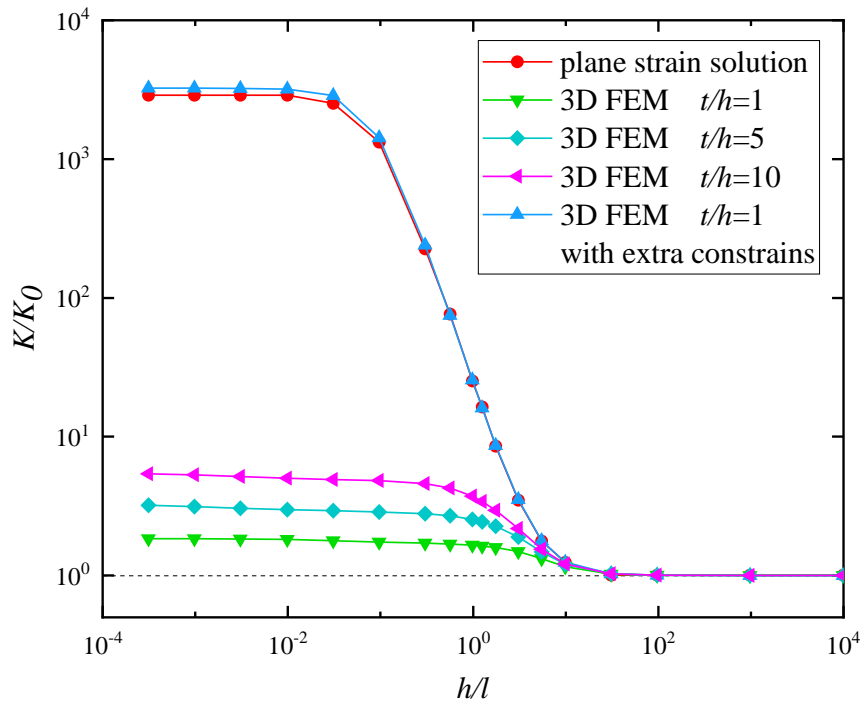
Figure 22. The stiffness of the fully fixed 3D cantilever thin beam
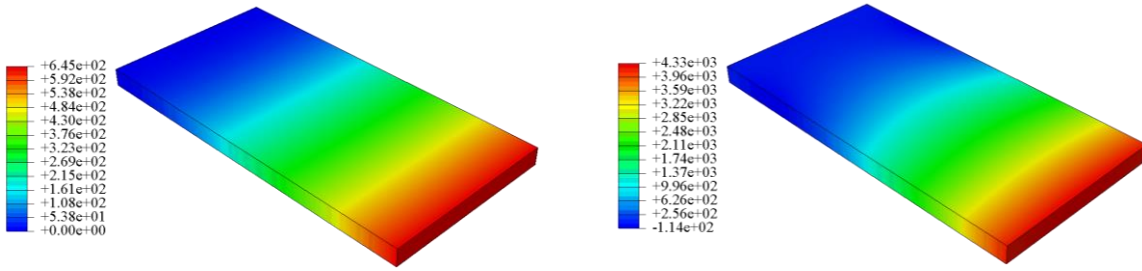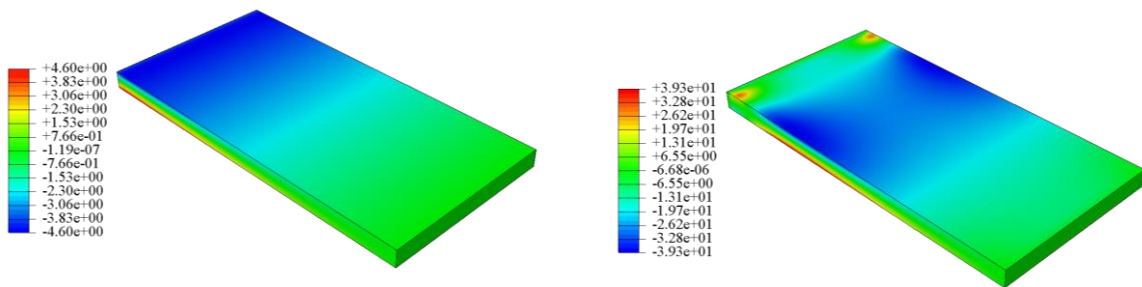
displacement v (mm)

stress σ_{xx} (MPa)
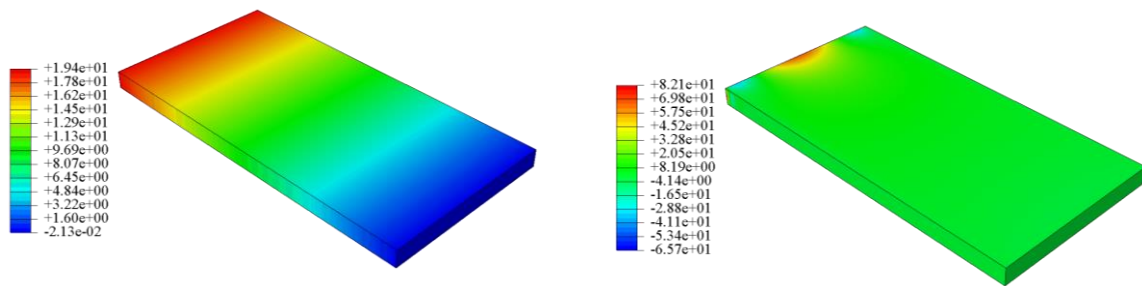
couple stress μ_{xz} (N/mm)

Figure 23. The displacement, stress and couple stress contours of the 3D cantilever beam (Left: with lateral constrains; Right: without lateral constrains)
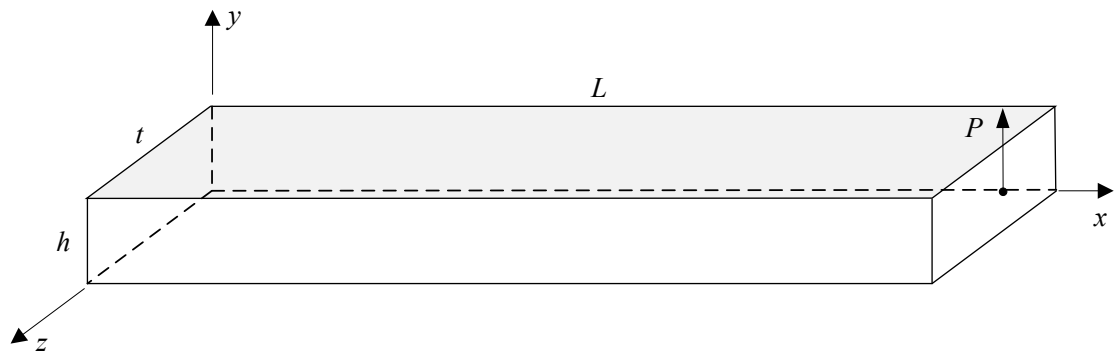
E=2.0MPa, v=0.0, P=1.0N, L/h=10, h=1.0mm
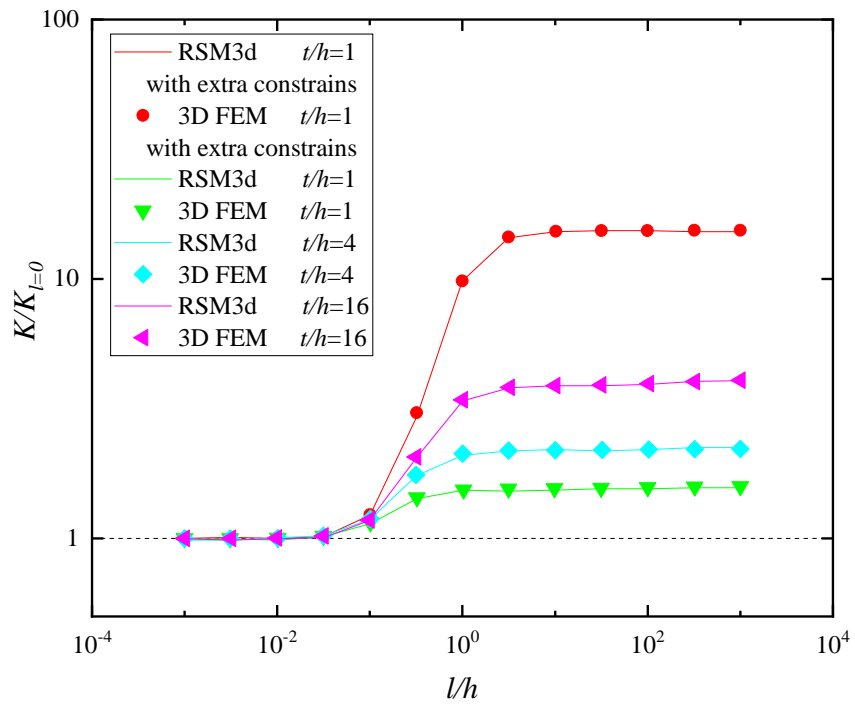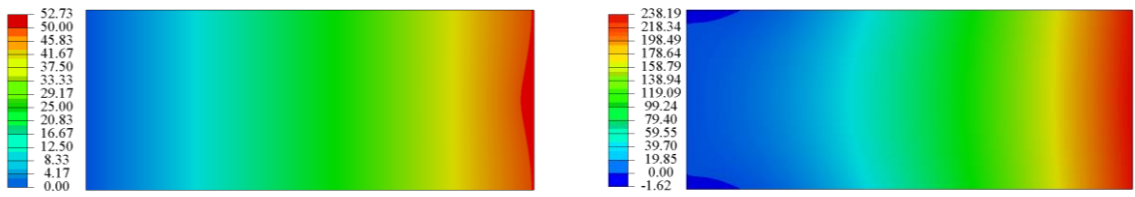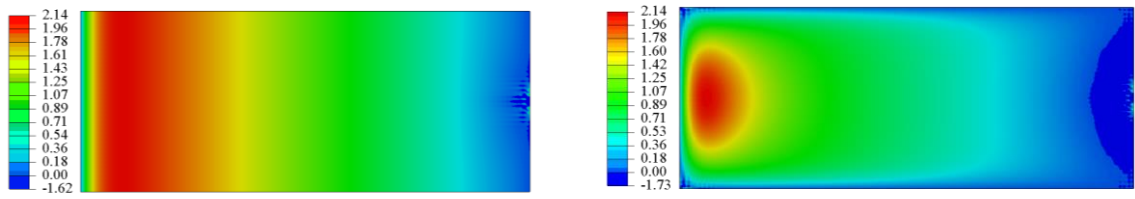
Figure 24. Another 3D cantilever thin beam

Figure 25. The stiffness of another 3D cantilever thin beam

displacement v (mm)

couple stress μ_{xz} (N/mm)

Figure 26. The displacement and couple stress contours of another 3D cantilever beam (Left: with lateral constrains; Right: without lateral constrains)